BILINGUAL
PUBLISHING CO.
Pioneer of Global Academics Since 1984

Semiconductor Science and Information Devices

Volume 4 • Issue 2 • October 2022 ISSN 2661-3212(Online)

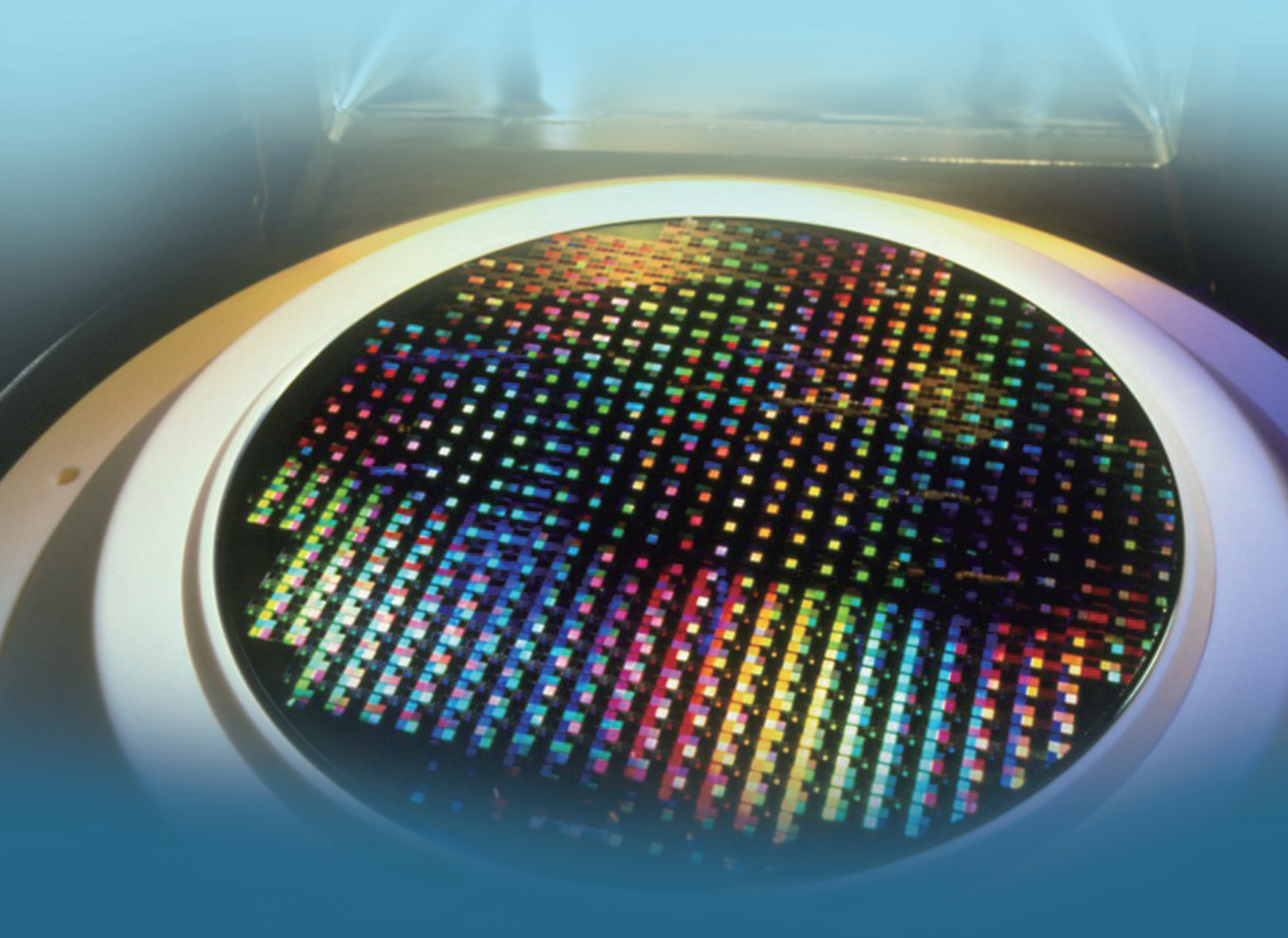

BILINGUAL PUBLISHING CO.
Pioneer of Global Academics Since 1984

Editor-in-Chief

Prof. Kasturi Vasudevan
Indian Institute of Technology Kanpur, India

Co-Editor-in-Chief

Prof. Jianhong Zhang
North China University of Technology

Editorial Board Members

Z heng Han, China
Elder Oroski, Brazil
Akram Sheikhi, Iran
Muhammad Sana Ullah, United States
Shuo Gao, China
Vajeeston Ponniah, Norway
Gennadiy Burlak, Mexico
Amalia N. Miliou, Greece
Fikret Yildiz, Turkey
Muhammad Waqas Iqbal, Pakistan
Niloufar Yavarishad, United States
Jie Song, United States
Prajoon Pavithran, India
Tseung-Yuen Tseng, Taiwan
Miao Zhou, China
Subash T D, India
Yuanqi Shen, United States
Wenhui YU, France
Mahdi Bahadoran, Iran
Yunyan Zhang, United Kingdom
Luca Persichetti, Italy
Patrick Dela Corte Cerna, Philippines
Ayuba John, Nigerian
Thanikanti Sudhakar Babu, Malaysia
Ahmed EL OUALKADI, Morocco
Luca Potì, Italy
Luka Strezoski, Serbia
Ren Li, Saudi Arabia
Shi-Hai Dong, Mexico
Basanta Kumar Roul, India
Feng Li, United States
Nihar R Pradhan, United States
Meysam Zareiee, Iran
Dongyan Zhang, China
Boualem Djezzar, Algeria
Suguo Huo, United Kingdom
Swayandipta Dey, Israel
Abbas Mohammed Selman, Iraq
Mebarka Daoudi, Algeria
Sergey Ivanovich Pokutnyi, Ukraine
Shubhakar Kalya, Singapore
Chun-Hsiang Chang, United States
Chunqing Wang, China
Waqar Mahmood, Pakistan
Rahima Nasrin, Bangladesh
Bikash Nakarmi, China
Hamed Dehdashti Jahromi, Iran
Muhammad Azeem, United Arab Emirates
Riadul Islam, United States
Francisco Bulnes, Algeria

Volume 4 Issue 2 • October 2022 • ISSN 2661-3212 (Online)

Semiconductor Science and Information Devices

Editor-in-Chief
Prof. Kasturi Vasudevan
Co-Editor-in-Chief
Prof. Jianhong Zhang

BILINGUAL PUBLISHING CO.
Pioneer of Global Academics Since 1984

Volume 4 | Issue 2 | October 2022 | Page1-44
Semiconductor Science and Information Devices

Contents

Articles

Review

BILINGUAL PUBLISHING CO.
Pioneer of Global Academics Since 1984

Semiconductor Science and Information Devices
https://ojs.bilpublishing.com/index.php/ssid

REVIEW

Signal and Power Integrity Challenges for High Density System-on-Package

Nathan Totorica Feng Li*

Department of Electrical and Computer Engineering, University of Idaho, Moscow, Idaho, 83844, USA

ARTICLE INFO

Article history
Received: 18 February 2022
Revised: 17 March 2022
Accepted: 28 March 2022
Published Online: 13 June 2022

Keywords:
System on package (SoP)
System in package (SiP)
System on chip (SoC)
Through silicon via (TSV)
Signal integrity
Power integrity
Thermal integrity

ABSTRACT

As the increasing desire for more compact, portable devices outpaces Moore's law, innovation in packaging and system design has played a significant role in the continued miniaturization of electronic systems. Integrating more active and passive components into the package itself, as the case for system-on-package (SoP), has shown very promising results in overall size reduction and increased performance of electronic systems. With this ability to shrink electrical systems comes the many challenges of sustaining, let alone improving, reliability and performance. The fundamental signal, power, and thermal integrity issues are discussed in detail, along with published techniques from around the industry to mitigate these issues in SoP applications.

1. Introduction

Portable electronics, IoT, and 5G continue to drive demand for smaller form factors with increased performance and reliability. While this trend is not new, many niche solutions have attempted to address it over the years. In the heyday of Moore's law, integrated circuit (IC) scaling was doubling roughly every two years. This gave rise to integrating whole modularized systems on a single IC, known as system-on-chip (SoC). While SoCs are widely used in many applications today, SoC comes with a lot of scaling and performance issues as Moore's law continues to slow down and integration of digital, RF, optical, and MEMS-based components into a single IC creates a much more complex fabrication process. In some specific market sectors, such as aerospace, the need for high-performance systems in small footprints is high. Still, low volume demand may not justify SoC solutions' considerable R&D and manufacturing costs. While modern transistor densities are at historical peaks, they have continued to

*Corresponding Author:
Feng Li,
Department of Electrical and Computer Engineering, University of Idaho, Moscow, Idaho, 83844, USA;
Email: fengli@uidaho.edu

DOI: https://doi.org/10.30564/ssid.v4i2.4475
Copyright © 2022 by the author(s). Published by Bilingual Publishing Co. This is an open access article under the Creative Commons Attribution-NonCommercial 4.0 International (CC BY-NC 4.0) License. (https://creativecommons.org/licenses/by-nc/4.0/).

drift from Moore's law. Apple's A14 mobile processor, for example, is reported at 11.8 billion transistors in an 88 mm^2 footprint (~134 million transistors per mm^2), and even with these impressive densities this SoC comes in less dense than what a 5 nm node would predict [1]. Innovation in package and system design has become increasingly important to address "Moore's Stress" [2].

Several decades ago, a modularized approach was taken to mimic SoC like behavior that instead combined several discrete components into a miniaturized system known as a multichip module (MCM) [3]. Innovation based on this idea has opened the door to many other types of advanced packaging technologies, such as system-in-package (SiP) and system-on package (SoP) that have shown as promising solutions to addressing "Moore's stress". Taking the MCM idea a step further, SiP brings multiple, potentially dissimilar, die into a single package, and expands the packages responsibility to include interconnection. This has enabled many creative solutions to package dissimilar ICs into single discrete packages [4-6]. Continued integration brought about SoP, bringing even more functionality into the package itself. SoP contains all interconnection, as well as embedded passive components on a single substrate. Packaging solutions are a new form of Moore's law that will continue to miniaturize systems and increase performance without relying strictly on transistor scaling. The role of packaging has expanded into new territory, with additional responsibilities on top of thermal dissipation, electromagnetic interference (EMI) shielding, and mechanical and environmental protection. These attributes have become especially desired in market sectors, such as medical, aerospace, and mobile devices, where size and weight are critically important.

Fundamental design challenges become increasingly detrimental to system performance as complexity grows, all while in ever-smaller footprints. Higher density layouts, along with faster edge rates, result in increased EMI that can generate crosstalk in the connector and signal traces. While SoP addresses many of the shortcomings seen amongst packaging solutions presented here, careful attention must be taken to address the fundamental signal, thermal, and power integrity issues.

2. Comparison of Advanced Packaging Solutions

Advances in package technology, such as MCM and SoC, originally pursued options that integrated functionality in a two-dimensional (2D) way. Continued innovation led to SiP and SoP expanding into three-dimensional (3D) territory by stacking discrete die vertically [7]. The history and background of the leading advanced packaging solutions are described in detail and compared in Table 1.

2.1 Multichip Module (MCM)

Innovation of Multichip modules was mainly driven by the needs of the aerospace industry, often called hybrid circuits where small footprints and high performance are a must [8]. Due to the low volume demand, novel solutions like MCM may be used instead placing discrete components onto a single substrate, two-dimensionally, facilitating interconnection. This technique is used when specialized components may be required and are not practical to integrate into a single, monolithic form. Components are physically positioned closer, which results in better signaling. Interconnects are typically built on ceramic (MCM-C), thin-film (MCM-D), or laminate (MCM-L) substrates, depending on the targeted application. The earliest form, MCM-C, is often used due to its higher capacitance and better power rail support. Improvements in areas like performance and cost quickly followed with deposited MCM-D and cheap laminates MCM-L. MCM-D allows use of reduced permittivity dielectrics that enable lower resistivity of interconnects, which in turn boosts performance. Additionally, since MCM-D uses photolithography methods smaller feature sizes are possible that enable higher density signal interconnections. Lastly the MCM-L approach utilizes commonly uses printed circuit board materials like FR-4 for interconnection and is generally the simplest approach. MCM proved very useful as a low-cost solution without forfeiting significant performance requirements. MCM modules employing low-temperature cofired ceramics (LTCC) and organic thin film have been remained especially popular in recent decades in RF and millimeterwave applications [9-11]. Multichip modules are the most generalized of the other advanced packaging solutions.

2.2 System-on-chip (SoC)

Integrating more functionality onto a single IC certainly has an understandable appeal. Smaller footprint, lighter weight, and lower power consumption are just a few of the desirable attributes that come with SoC designs. Execution speeds are extremely fast with minimal trace lengths and propagation latency between logic blocks. If implemented effectively, SoC offers the most cost-effective system solution that is high volume manufacturable. While transistor scaling remained closely in step with Moore's law, this seemed to be the solution of the future. However, as systems grow more complex many challenges that accompany SoC are realized when trying to incorporate a variety of functionalities, such as RF, analog, digital, or optics, all into a single IC. Further, integrating simple passives onto IC incurs a large die size hit, and fabricating high Q-factor passives for RF applications is extremely difficult [12]. Other drawbacks include the fact that complex, low-yielding fabrication processes in certain blocks of the SoC can cause entire chip to be scrapped. Despite these drawbacks, there are many advantages to combing similar blocks into SoC, in conjunction with other SiP or SoP systems to realize full system functionality.

2.3 System-in-package (SiP)

SiP can incorporate 2D or 3D layouts, with the latter configuration reaching near chip-scale package sizes. 3D stacking techniques are often used with highly regular die as is generally the case for memory ICs [13,14]. The SiP solution can also exploit the ability to place dissimilar, high-yielding die into a single discrete package. Commonly, high-density memory like High Bandwidth Memory (HBM) is packaged along with computational Application Specific Integrated Circuits (ASIC) [15]. This stacked configuration can use a variety of high-density interconnect (HDI) technologies, from wire bonding, through silicon via (TSV) or flip-chip techniques for I/O interconnection. Many 3D stacking configurations rely on TSV or wire bonding, but as need for more I/O pin counts increase, fanout techniques are being employed to meet these high bandwidth requirements using wafer level packaging (WLP) [16]. Some other techniques exploit cheaper redistribution layers (RDL) to facilitate interconnection [17], which eliminates need for expensive WLP equipment and removes costly interposer TSV process steps. The flexibility to customize SiP systems to the application and manufacturing needs is a major reason for its widespread adoption. SiP designs are often able to be treated like a normal, single packaged IC which poses a big advantage in assembly simplification compared to MCM.

2.4 System-on-package (SoP)

Taking a step further, SoP combines SiP style stacked die with integrated passive elements, overcoming many of the disadvantages faced by all three MCM, SoC, and SiP techniques. Integrated passive components can utilize thin-film deposition techniques that allow thinner, more reliable performance than typical discrete passives. SoP effectively creates a complete PCB functionality into a single discrete footprint. The reduced signaling path between die decreases trace losses, which is exacerbated in RF applications [2]. Generally, inductors, capacitors, and antennas are much more easily realized on package substrate than on silicon, especially for high Q-factor requirements. Additionally, this allows more flexibility than in an SoC design. Ultimately, many of the aspirations of SoC can be achieved using SoP techniques. While SoP is very similar to SiP in concept, SoP promises much more functionality. Subsequently, this increased complexity means additional challenges must be addressed to realize these benefits [18]. Due to these challenges SoP has been slow to take hold in industry. In recent years however, 5G has created a resurgence of attention around SoP, with many applications exploiting mmWave based 5G frequencies to build extremely compact RF components for a highly integrated SoP solution [19-21].

Table 1. Electronic package technology comparison

Package Technology	Advantages	Disadvantages
MCM	- Modularized - Robust - Cost effective	- Larger footprint
SoC	- Smallest footprint - Highest speed - Low power	- Long design/ verification cycles - Difficult testability - Potentially low yield
SiP	- Simpler design & verification - Shorter time to market - 2.5/3D stacking	- Complex packaging equipment/assembly
SoP	- Embedded (thin film) passives - Flexibility - Small system footprint - 2.5/3D stacking	- More complex than SiP - SI/PI challenges

3. Signal and Power Integrity Issues

Along with the desire for smaller, more compact electrical systems, demand for faster speeds is also increasing. Faster speeds, and in turn, faster signal rise times bring a myriad of signal integrity issues. Commonly referred to as dV/dt and dI/dt noise, the faster signals change, the more EMI and subsequent noise is generated. Along with these challenges, designers have less and less space for routing traces. Traces are packaged closer together in package and PCB, resulting in very high-density routing and higher coupling between signal traces. Classic signal integrity problems become more apparent as systems get larger and timing margins get smaller. The most common issues are discussed in the following sections.

3.1 Reflections

Through a signals entire path, it will see impedance at every point along the way. One of the most common signal integrity issues that arise in high-speed systems is signal reflection [22]. Reflections occur when there is a sudden change in impedance and is commonly simplified as an equivalent transmission line feeding a load impedance, as seen in Figure 1.

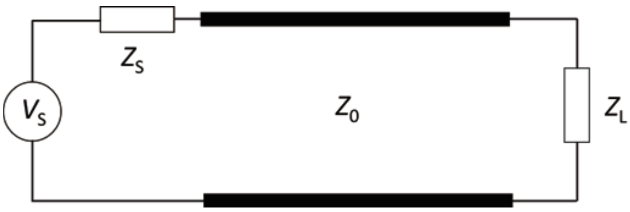

Figure 1. Transmission line feeding load impedance

This relationship is described in Equation (1) to show that the closer the impedances are matched, the smaller the reflection will be.

$$\Gamma = \frac{Z_L - Z_0}{Z_L + Z_0} \tag{1}$$

Additionally, this can be caused by any change in signal medium or trace geometry. Typical examples include vias, edge connectors, or solder joints. Signals that see an extremely high impedance, like an open, will have 100% reflection with a 0° phase shift in the signal. The other extreme is that if the signal sees zero impedance, like a short, 100% of the signal will be reflected, but this time with a 180° phase shift. Since reflections are a well-known issue, designers have come up with different techniques to minimize them. The primary way is to add termination to signaling paths. A few examples of terminations schemes include series, parallel, or double termination. For series termination, reflections will bounce off the receiver side and terminate at the transmitter side. Series termination can be useful to eliminate crosstalk effects. Parallel termination is a very common termination scheme where the transmitted signal will terminate at the receiving side and can be done by either terminating transmission line to the power supply VDD or to the ground Double termination can be parallel terminations on both source and receiver side, or a combination of series and parallel termination schemes. Double termination schemes are often used in high-speed, high performance serial link designs [23].

3.2 Crosstalk

Change in current or voltage through a conductive medium will create changing electric and magnetic fields. If a signal is propagating down one line, known as the aggressor line, and the magnetic field lines intersect another conductive medium, known as the victim line, a voltage and resulting current will be generated on the victim line. The intersecting magnetic field creates a relationship known as mutual inductance (L_m) between the two conductors, and the intersecting electric field creates mutual capacitance (C_m). The resulting signal generated on the victim line through coupling to the aggressor line is known as crosstalk. This can cause issues when the layout for two sensitive signal paths is extremely close together. The individual voltages are defined by Equations (2) and (3).

$$\Delta V_L = L_m * dI/dt \tag{2}$$

$$\Delta V_c = C_m * dV/dt \tag{3}$$

Typically for transmission lines with long, wide return paths, the amount of mutual inductance and mutual capacitance is comparable. However, for non-uniform structures, like connectors or pins, inductive coupling dominates [24]. In the case of transmission lines, the crosstalk manifests differently at the near end versus the far end. This is known as near-end crosstalk (NEXT) versus far-end crosstalk (FEXT).

The polarity and magnitude can be different between the NEXT and FEXT noise signals, demonstrated in Figure 2, and is dependent on which type of EMI is dominant in generating the noise. The mutual inductive coupling will create a wave that propagates in either direction, one towards the far end and one towards the near end that are opposite in polarity. The mutual capacitance will also generate a wave in either direction but with the same polarity. The combination of these interactions will describe how the FEXT and NEXT noise will look at either end of the victim transmission line.

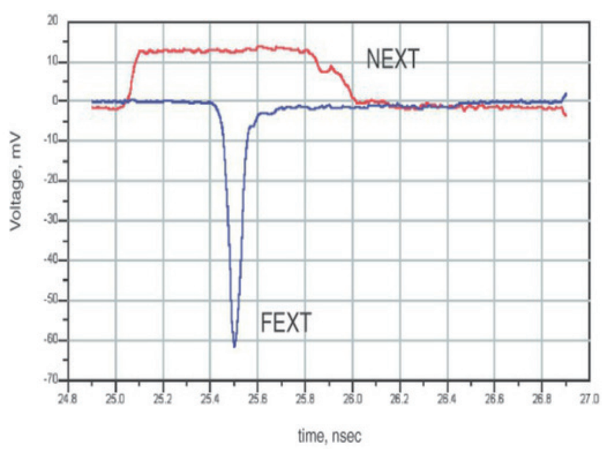

Figure 2. Measured noise on the quiet line when the active line is driven with a 200-mV, 50-psec rise-time signal. Measured with an Agilent DCA TDR and GigaTest Labs Probe Station [24].

3.3 Power Distribution Network (PDN)

The power distribution network is one of the most important pieces of the system. Careful attention must be paid to the PDN to ensure a low impedance profile across a broad frequency spectrum. Ideally, a chip expects a constant near-flat DC voltage supply. High inductance in power and ground connections can cause unwanted power rail fluctuations due to the inability for PDN to respond to quick current draw, causing a voltage drop. This is especially true with many drivers toggling simultaneously, often called simultaneous switching noise (SSN) or delta I noise. The delta I noise is described by Equation (4) where L_{eff} is the PDN effective inductance and N is the number of switching drivers.

$$\Delta V = N\, L_{eff} \frac{\Delta i}{\Delta t} \tag{4}$$

This effect is nearly impossible to avoid but ensuring impedance remains below target values across the bandwidth of the design is the only way to guarantee correct system operation.

4. SoP Design Challenges

Regardless of the package methodology, traditional design issues like crosstalk, impedance mismatch, rail collapse, and thermal emission will be present, if not exacerbated with tighter layouts and faster clock speeds. Since SoP designs share a subset of design challenges as SiP, many real-world solutions are used interchangeably to illustrate how to mitigate these issues. For example, Qualcomm's newer Snapdragon series expands SoC design to a SiP, supporting up to 1.8 GHz per core, with over 400 individual components. The Snapdragon SiP contains memory, RF, audio, and more all in one compact footprint, easily integrated into mobile phone systems [25]. For applications such as this, traditional management techniques like increased spacing or reduced signal edge rate may not be sufficient or possible under the size and speed specifications. Additionally, a well-known problem for packaged systems is the Known Good Die (KGD) issue. If SoP or other stacked die packages are built with one defective die, then the other good die and components may be scrapped along with it. This can pose yield issues for SoP designs, resulting in high fabrication expenses. Sufficient die level testing is necessary to avoid this issue. Many of the techniques discussed in this section will help mitigate some other common issues for a more robust SoP system design.

4.1 Signal Integrity

Inherent benefits of SoP include integration of interconnects into the package, thin-film construction of passive components, and easier integration of dissimilar die. Reducing overall signaling length helps to improve signal integrity. Interconnect paths can use a variety of options like wire bonding or TSV techniques. While TSV is more expensive than wire bonding, it offers shorter interconnects and improved signaling. Shorter channel lengths give less distance for parallel traces to couple, reducing crosstalk and insertion loss. As previously discussed, reduced signaling loss is a major benefit, especially for RF modules in mobile devices where prolonged battery life is a major benchmark. Additionally, SoP enables the ability to fabricate thin-film passive components. Thin films enable smaller, better-performing passive devices compared to standard discrete components. Fabricating high-Q passive components is extremely difficult on a die and takes a large amount of die real estate.

Post silicon issues are costly, making simulations key to proactive system debugging. Proper simulation allows issues to be found well before anything is physically made. Simulating entire systems can be difficult and resource-intensive, though. If that expense is not an option, using intuition built off the signal and power integrity concepts discussed previously can help pinpoint worst-case susceptible signal paths. As discussed by Yang et al. [26], looking at a handful of these most critical paths help build confidence that the overall design will meet specifications. Generally, all the most sensitive paths, such as clock trees, should be examined thoroughly in simulation.

A technique that is commonly used for transmitting signals over longer traces (i.e. chip to chip) is pulse shaping [27]. The idea is to shape the signal in such a way as to better interact with the characteristics of the channel and transmit more accurately to the receiver. This idea could potentially be implemented to decrease the signal rise time by using a more sinusoidal shaped wave to eliminate some of the highest order harmonics associated with a square wave. This could help reduce some of the dV/dt, dI/dt noise that is generated by faster signal switching. Generally, slower rise times that still meet specifications (e.g., setup and hold timings) are always better from an EMI perspective.

4.2 Power Integrity

For both board and package level PDN, the overall impedance must be kept under target value through the entirety of the operating frequencies. Especially, low return path inductance reduces the effects of SSN and ground bounce. Wider conductors for power and ground planes will help reduce loop inductance. The threat of rail collapse can be mitigated by using decoupling capacitors strategically sized and placed to lower PDN impedance, as well as compensate for voltage droop caused by simultaneous switching [28]. Typically, several different types of decoupling capacitors are used in PDN design (bulk, local, package, embedded, and on-die) to cover specific frequency ranges. A comprehensive pre and post route power integrity analysis is outlined [29] to provide better performance of PDN. A critical piece in the study is to include implications of capacitor effective series resistance (ESR) and effective series inductance (ESL); if left out of the analysis, these can have unforeseen effects at the high frequencies. The technique outlined by Venkatesan et al. [14] uses embedded TSV-Caps to further tune impedance below the target levels at the high frequency range. MIM or trench capacitors are often embedded into interposer to tune at these high frequency harmonics but require significant silicon area and additional process steps. The TSV-Cap approach embeds the capacitor around the TSV structure in the pitch between adjacent TSVs. The technique, shown in Figure 3, allows increase of bandwidth with minimal increase in silicon area required.

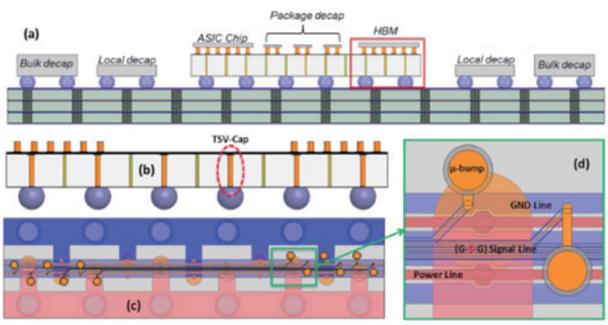

Figure 3. (a) ASIC-HBM packaging illustration. (b) The interposer elevation view. (c) Interposer cluster interconnect. (d) PI/SI and GND line [14].

Additionally, the effects of the TSV-Cap on crosstalk were analyzed to ensure that these structures do not cause unwanted noise on signal lines due to coupling of power lines through the TSV-Cap structures. Comparing insertion and return loss metrics between device with and without TSV-Cap shows comparable performance for insertion loss at low frequencies and a general improvement at higher frequencies, with return loss generally improved across entire frequency range.

4.3 Thermal Management

Thermal management is extremely important to consider when designing any system, and this is especially true as SoP die stacks grow higher and bandwidths meet 5G specifications. A widely noticed trend in CPU clock speeds is that newer generations are not making the same massive jumps in operating speed as seen in the past. This complex problem is deeply involved with transistor physics and physical size, but an additional factor is a difficulty cooling for clock speeds greater than 3 GHz-5 GHz. Thermal management has become an integral part of package and system design that cannot be ignored. Although thermal dissipation is one of the package's most important roles, thermal considerations need to start with electrical design. Excessive current density generates heat, leading to electrical failure or even mechanical package warping [28].

While heat generation is impossible to avoid, novel thermal management solutions are pursued to ensure adequate cooling for stacked die. During the design phase, transient thermal simulations, as discussed by Yoo et al. [30], ensure systems have a relatively even heat distribution across workloads. Careful attention to the order of the stack up, as presented by Mathur [31], can mitigate the increased heat generated from 3D stack configurations. Using a 3 GHz CPU as a test vehicle, modularized chiplets are stacked three-dimensionally in a logic-over-memory configuration. Comparison between a stacked configuration where thermal implications are considered versus when they are not showing a significant difference in overall heat experienced. A pre-simulated stacked design may experience half as much temperature increase as compared to a design where thermal implications are not considered. When compared to a traditional 2D design, the thermal efficient 3D design may experience as little as a 6 °C increase while decreasing the footprint by 23%. For applications that can tolerate the temperature increase, this is a significant reduction in space occupied. In general, these studies echo the importance of thorough simulation to understand thermal implications.

Concentrated heat areas can cause issues, especially at the transistor level where elevated temperatures cause higher leakage currents and increased scattering. A major consideration for 3D configurations is the possibility of different max temperature ratings, as is commonly seen with stacked logic and DRAM. For example, an ASIC may be rated up to 125 °C while HBM is only rated to 95 °C [32]. Ensuring all devices are operating within specification is a must to avoid throttling and subsequent performance hits. Proper cooling will increase the longevity and reliability of the system.

Thermal bottlenecks tend to appear towards the center and lower stacked die in a 3D configuration. Solutions to avoid this type of bottleneck, like the ICE-SiP technique as presented by Kim et al. [33], use highly thermal conductive "chimneys" to dissipate heat from the inner layers to a heat sink, as depicted in Figure 4. In this example, a DRAM die is stacked on a computational ASIC. The ICE-SiP technique shifts the DRAM off center to provide room for an alternative, lower thermally resistant path made of silver (Ag) for heat to transfer instead of dissipating through the DRAM. Other configurations may use silicon (Si) instead of silver due to its higher thermal conductivity, ~120 W/mK versus ~50 W/mK, respectively. However, based on simulation results, the Ag-based chimney performed best, coupled with high-K epoxy compound molding (EMC). In contrast, the Si chimney required an adhesive to bond to the die and ultimately suffered from the low thermal conductivity of the adhesive.

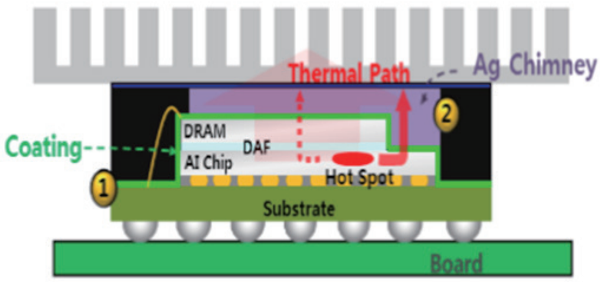

Figure 4. Geometry of the "ICE-SiP" [33].

Increasingly, more advanced methods of thermal management are being researched for next generation electronics, including novel approaches in magnetic cooling [34] and nanofluids [35]. Nanofluids are a form of liquid cooling that employs nano particles suspended in a base fluid to increase thermal conductivity beyond what is achievable with traditional air or water mediums. The particles are often a metal but as described by Zumbühl [34], many different compounds have been researched, including carbon-based nanotubes. The base fluid is typically comprised of water, ethanol glycol, or oil. Generally, these results have shown very promising although this technique has not yet been widely adopted in applications.

5. Conclusions

The trend toward more compact and mobile systems is likely to continue, if not grow, in upcoming years. SoP innovation has offered a promising solution to help with these scaling trends. While the fundamental signal, power, and thermal challenges are only going to get harder to overcome, the solutions discussed here can help mitigate these problems for more robust, reliable products.

Conflict of Interest

There is no conflict of interest.

References

[1] Patel, D., 2020. Apple's A14 packs 134 million transistors/mm², but falls short of TSMC's density claims. https://semianalysis.com/apples-a14-packs-134-million-transistors-mm2-but-falls-far-short-of-tsmcs-density-claims/. (Accessed 26 March 2022)

[2] Dai, W.W., 2016. Historical perspective of system in package (SiP). IEEE Circuits and Systems Magazine. 16(2), 50-61. DOI: https://doi.org/10.1109/MCAS.2016.2549949

[3] Rinebold, K., Felton, K., 2017. Designing and Integrating MCM/SiP Packages into Systems PCBs. https://www.3dincites.com/wp-content/uploads/mentorpaper_101401.pdf. (Accessed 26 March 2022).

[4] Lian, F., Wang, D., Chiu, R., et al., 2019. Innovative packaging solutions of 3D integration and system in package for IoT/wearable and 5G application. IEEE 21st Electronics Packaging Technology Conference (EPTC). pp. 515-518. DOI: https://doi.org/10.1109/EPTC47984.2019.9026573

[5] Elisabeth, S., 2019. Advanced RF packaging technology trends, from WLP and 3D integration to 5G and mmwave applications. International Wafer Level Packaging Conference (IWLPC) pp. 1-5. DOI: https://doi.org/10.23919/IWLPC.2019.8914089

[6] Wase, Y.S., Li, F., 2017, Technology review of system in package. In Additional Conferences (Device Packaging, HiTEC, HiTEN, & CICMT). pp. 1-20.

[7] Tummala, R.R., 2004. SOP: what is it and why? A new microsystem-integration technology paradigm-Moore's law for system integration of miniaturized convergent systems of the next decade. IEEE Transactions on Advanced Packaging. 27(2), 241-249. DOI: https://doi.org/10.1109/TADVP.2004.830354

[8] Ulrich, R.K., Brown, W.D., 2006. Advanced Electronic Packaging, IEEE. Ch.14. DOI: https://doi.org/10.1109/9780471754503.ch14

[9] Carchon, G., Vaesen, K., Brebels, S., et al., 2001. Multilayer thin-film MCM-D for the integration of high-performance RF and microwave circuits. Transactions on Components and Packaging Technologies. 24(3), 510-519. DOI: https://doi.org/10.1109/6144.946500

[10] Foure, J., Dravet, A., Cazenave, J., et al., 1995. Mixed technologies for microwave multichip module (MMCM) applications-a review. IEEE NTC,Conference Proceedings Microwave Systems Conference. pp. 73-81. DOI: https://doi.org/10.1109/NTCMWS.1995.522865

[11] Shafique, M.F., Robertson, I.D., 2015. A two-stage

process for laser prototyping of microwave circuits in LTCC technology. IEEE Transactions on Components, Packaging and Manufacturing Technology. 5(6), 723-730.
DOI: https://doi.org/10.1109/TCPMT.2015.2434273

[12] Li, X., Gu, L., Wu, Z., 2008. (INVITED) High-performance RF passives using post-CMOS MEMS techniques for RF SoC. IEEE Radio Frequency Integrated Circuits Symposium. pp. 163-166.
DOI: https://doi.org/10.1109/RFIC.2008.4561409

[13] Jun, H., Cho, J., Lee, K., et al., 2017. HBM (High Bandwidth Memory) DRAM technology and architecture. IEEE International Memory Workshop (IMW). pp. 1-4.
DOI: https://doi.org/10.1109/IMW.2017.7939084

[14] Venkatesan, S., Aoulaiche, M., 2018. Overview of 3D NAND technologies and outlook. Non-Volatile Memory Technology Symposium (NVMTS). pp. 1-5.

[15] Apriyana, A.A., Ye, L., Seng, T.C., 2019. TSV with embedded capacitor for ASIC-HBM power and signal integrity improvement. IEEE SOI-3D-Subthreshold Microelectronics Technology Unified Conference (S3S). pp. 1-2.
DOI: https://doi.org/10.1109/S3S46989.2019.9320698

[16] Tseng, C.F., Liu, C.S., Wu, C.H., et al., 2016. InFO (Wafer Level Integrated Fan-Out) Technology. IEEE 66th Electronic Components and Technology Conference (ECTC). pp. 1-6.
DOI: https://doi.org/10.1109/ECTC.2016.65

[17] You, S.H., Jeon, S., Oh, D., et al., 2018. Advanced fan-out package SI/PI/thermal performance analysis of novel RDL packages. IEEE 68th Electronic Components and Technology Conference (ECTC). pp. 1295-1301.
DOI: https://doi.org/10.1109/ECTC.2018.00199

[18] Wan, L., 2018. SiP/SoP technology and its implementation. International Conference on Electronic Packaging Technology & High Density Packaging. pp. 1-3.
DOI: https://doi.org/10.1109/ICEPT.2008.4606942

[19] Zhou, L., Feng, W., Wang D., et al., 2020. A compact millimeter-wave frequency conversion SOP (System on Package) module based on LTCC technology. IEEE Transactions on Vehicular Technology. 69(6), 5923-5932.
DOI: https://doi.org/10.1109/TVT.2020.2989451

[20] Craton, M.T., Konstantinou, X., Albrecht, J.D., et al., 2021. Additive manufacturing of a W-band System-on-Package. IEEE Transactions on Microwave Theory and Techniques. 69(9), 4191-4198.
DOI: https://doi.org/10.1109/TMTT.2021.3076066

[21] Georgiadis, A., Tentzeris, M., 2019. Achieving fully autonomous system-on-package designs: an embedded-on-package 5G energy harvester within 3D printed multilayer flexible packaging structures. IEEE MTT-S International Microwave Symposium (IMS). pp. 1375-1378.
DOI: https://doi.org/10.1109/MWSYM.2019.8700931

[22] Johnson, J., Graham, M., 1993. High-Speed Digital Design: A handbook of black magic. Prentice Hall, Upper Saddle River, NJ.

[23] Palermo, S., 2021. Termination, TX driver, & multiplexer circuits. ECEN 720. Class Lecture, School of Electrical and Computer Engineering, Texas A&M University. College Station.

[24] Bogatin, E., 2018. Signal and Power Integrity - Simplified. Prentice Hall.

[25] Qualcomm. Snapdragon system-in-package. https://www.qualcomm.com/products/snapdragon-system-package. (Accessed 27 March 2022)

[26] Yang, Z., Gao, Y., Li, S., et al., 2021. Research on SiP signal integrity based on Ansys SIwave in wearable medical systems. 22nd International Conference on Electronic Packaging Technology (ICEPT). pp. 1-4.
DOI: https://doi.org/10.1109/ICEPT52650.2021.9567976

[27] Vasudevan, K., 2010. Digital communications and signal processing. Universities Press, Second edition.

[28] Wang, L., Zhang, Y., Zhang, G, et al, 2010. Power integrity analysis for high-speed PCB. First International Conference on Pervasive Computing, Signal Processing and Applications. pp. 414-418.
DOI: https://doi.org/10.1109/PCSPA.2010.106

[29] Chandana, M., Mervin, J., Selvakumar, D., 2015. Power integrity analysis for high performance design. International Conference on Control, Electronics, Renewable Energy and Communications (ICCEREC). pp. 48-53.
DOI: https://doi.org/10.1109/ICCEREC.2015.7337052

[30] Yoo, J., Im, Y., Lee, H., et al., 2020. Impact of Chip, Package, and Set Design on Transient Temperature in Mobile Application. 19th IEEE Intersociety Conference on Thermal and Thermomechanical Phenomena in Electronic Systems (ITherm). pp. 229-235.
DOI: https://doi.org/10.1109/ITherm45881.2020.9190945

[31] Mathur, R., Chao, C.J., Liu, R., et al., 2020. Thermal analysis of a 3D stacked high-performance commercial microprocessor using face-to-face wafer bonding

technology. IEEE 70th Electronic Components and Technology Conference (ECTC). pp. 541-547. DOI: https://doi.org/10.1109/ECTC32862.2020.00091

[32] Micron Technology, Inc., 2018. High bandwidth memory with ECC. HMB2E Datasheet. https://media-www.micron.com/-/media/client/global/documents/products/data-sheet/dram/hbm2e/8gb_and_16gb_hbm2e_dram.pdf?rev=dbfcf653271041a497e5f1bef1a169ca. (Accessed 27 March 2022)

[33] Kim, S.K., Oh, D.S., Hwang, S., et al., 2019. Electrical and thermal co-analysis of thermally efficient SiP for high performance applications. Electrical Design of Advanced Packaging and Systems (EDAPS). pp. 1-3. DOI: https://doi.org/10.1109/EDAPS47854.2019.9011675

[34] Zumbühl, D., 2018. Magnetic cooling of nanoelectronic chips. Tech Briefs, University of Basel, Switzerland. https://www.techbriefs.com/component/content/article/tb/pub/briefs/electronics-and-computers/28564. (Accessed 27 March 2022)

[35] Bahiraei, M., Heshmatian, S., 2018. Electronics cooling with nanofluids: a critical review. Energy Conversion and Management. 172, 438-456. DOI: https://doi.org/10.1016/j.enconman.2018.07.047

BILINGUAL PUBLISHING CO.
Pioneer of Global Academics Since 1984

Semiconductor Science and Information Devices
https://ojs.bilpublishing.com/index.php/ssid

ARTICLE

Convection Heat Transfer from Heated Thin Cylinders Inside a Ventilated Enclosure

Ali Riaz[1] Adnan Ibrahim[2*] Muhammad Sohail Bashir[3] Muhammad Abdullah[1] Ajmal Shah[1] Abdul Quddus[1]

1. Department of Mechanical Engineering, Pakistan Institute of Engineering and Applied Sciences, Islamabad, 45650, Pakistan
2. School of Engineering Science, University of Science and Technology of China, Hefei, Anhui, 230027, China
3. Hefei National Laboratory for Physical Sciences at the Microscale, CAS Key Laboratory of Soft Matter Chemistry, Department of Polymer Science and Engineering, University of Science and Technology of China, Hefei, Anhui, 230026, China

ARTICLE INFO

Article history
Received:16 May 2022
Revised: 20 June 2022
Accepted: 29 June 2022
Published Online: 15 July 2022

Keywords:
Experimentation
Ventilated enclosures
Convection heat transfer
Dimensionless data

ABSTRACT

Experimental study was conducted to determine the effect of velocity of axial fan, outlet vent height, position, area, and aspect ratio (h/w) of ventilated enclosure on convection heat transfer. Rectangular wooden ventilated enclosure having top and front transparent wall was made up of Perspex for visualization, and internal physical dimensions of box were 200 mm × 200 mm × 400 mm. Inlet vent was at bottom while outlet vents were at the side and top wall. Electrically heated cylindrical heat source having 6.1 slenderness ratio was fabricated and hanged at the centre of the enclosure. To calculate heat transfer rates, thermocouples were attached to the inner surface of heat source with silica gel. Heat source was operated at constant heat flux in order to quantify the effect of velocity of air on heat transfer. It was observed that average Nusselt number was increased from 68 to 216 by changing velocity from 0 to 3.34 m/s at constant modified Grashof number i.e. 5.67E+09. While variation in outlet height at the front wall did not affect heat transfer in forced convection region. However, Nusselt number decreased to 5% by changing the outlet position from top to the front wall or by 50% reduction in outlet area during forced convection. Mean rise in temperature of enclosure increased from 8.19 K to 9.40 K by increasing aspect ratio of enclosure from 1.5 to 2 by operating heat source at constant heat flux i.e. 541.20 w/m^2.

*Corresponding Author:
Adnan Ibrahim,
School of Engineering Science, University of Science and Technology of China, Hefei, Anhui, 230027, China;
Email: adnan36@mail.ustc.edu.cn

DOI: https://doi.org/10.30564/ssid.v4i2.4719

Copyright © 2022 by the author(s). Published by Bilingual Publishing Co. This is an open access article under the Creative Commons Attribution-NonCommercial 4.0 International (CC BY-NC 4.0) License. (https://creativecommons.org/licenses/by-nc/4.0/).

1. Introduction

Convection heat transfer from cylindrical heated surfaces inside the ventilated enclosure is of practical importance related to designing of enclosure of electronic equipments and ventilation of building. From design point of view, aspect ratio of enclosure, position and area of vents, velocity of fan in case of forced convection are critical variables. These parameters should be opted in such a way that it yields in maximum cooling and optimum electrical energy consumption. Due to recent development in electronics industry, reliability of system is hugely dependent on working of its electronic component. Literature shows that main cause of electronic equipment failure is rise in temperature [1].

Ali Riaz et al. studied effect of heat source height inside the ventilated enclosure on mean rise in temperature numerically. This study suggested that heat source should be at minimum height relative to the base of enclosure or at maximum height relative to the outlet position of the enclosure to achieve maximum cooling [2,3]. Basavaraj Kusammanavar et al. numerically studied the effect of heat source position on natural convection in a square cavity. Two dimensional simulations were performed in ANSYS Fluent to expedite a problem. Main finding of the study is that heat transfer increases by splitting heat source [4]. Chavan S. and Sathe A. performed three dimensional numerical simulations to study the impact of inter board spacing and heat dissipation rate on heat transfer and flow field inside the enclosure. Through proper placement of electronic component temperature of enclosure can be reduced from 3 ºC to 5 ºC [5].

Fahad Sadekin Zaman et al. studied velocity and temperature fields inside the enclosure having multiple discrete heat sources [6]. V.C. Mariani and L.S. Coelho studied effect of aspect ratio of open enclosure and temperature difference of vertical walls and internal heat source intensity on Nusselt number [7]. Luiz Joaquim C.R. and Henor Arthur S. studied influence of internal heat source in naturally ventilated offices. They found that cross ventilation is more useful as compared to unilateral [8]. Masaru I. and Shinji N. experimentally studied effect of outlet area and height on natural convection inside the ventilated enclosure. To accomplish this study, they fabricated ventilate enclosure having dimensions: 220 mm × 230 mm × 310 mm, and heat source. At the end, results are reported in the form of dimensionless number [9].

Norma Alejandra R.M. et al. modelled room as ventilated cavity and performed numerical simulations on ANSYS Fluent 6.3 by applying k-ε turbulence model along with non-uniform grid. Results are reported in dimensionless form [10]. Satish K.A. and A.N. Mathur studied combined effect of forced and natural convection in a ventilated enclosure with different outlet vents arrangements. Surface temperature of bottom heated surface was recorded against different values of Grashof and Reynold number and outlet vent configuration [11]. Azhar Kareem Muhammad et al. performed experiments to determine heat transfer from cylindrical heated surface inside the ventilated enclosure. Experiments were performed for the range of Ra 3.47×10^3 to 5.66×10^4, aspect ratio $11 \leq L/D \leq 22$ and inclination angle of heat source 0º to 90º [12].

S.K. Ajmera and A.N. Mathur studied the effect of mixed (free and forced) convection heat transfer in ventilated enclosure by changing ventilation arrangements. For this, they performed numerical simulations by flush mounted heat source at bottom wall. Average heat source temperature at different value of Richardson number was recorded for different combination of vents [13]. E. Bilgen and A. Muftuoglu observed that optimum position of heat source inside the ventilated enclosure depends upon ventilation ports arrangements rather than Richardson number. Furthermore, they plotted Nusselt number as a function of Richardson number [14].

2. Motivation for the Present Research

Main purpose of manufacturing and fabricating indigenous experimental setup was to study the critical parameters of ventilated enclosure on convection heat transfer. Number of research studies are available on geometric effect in natural convection, while limited data is available in forced convection. This study can be used in designing of enclosures for electronics systems or ventilation of building. It can be noticed by studying literature that experimental data is limited and mostly numerical findings are available, therefore, this study is addition to experimental results archive. Furthermore, this could be used as a bench mark for numerical simulations and formulation of empirical correlation.

3. Energy Balance

Net heat generated from cylindrical heat source is equal to convection, radiation and heat loss from endcaps as shown in Equation (1).

$$Q_{total}=+Q_{convection}+Q_{radiation}+Q_{loss} \tag{1}$$

Radiation heat transfer can be calculated through Stephen Boltzman law, heat losses through Fourier law of heat conduction while convection heat transfer through Newton's law of cooling. Net heat generated was equal to the product of current and voltage.

4. Experimental Setup

Rectangular ventilated enclosure having internal dimensions: 200 mm × 200 mm × 400 mm, was manufactured. Cylindrical heat source having 6.10 slenderness ratio was hanged at the center of enclosure by strings. There were four outlet vents and one inlet vent in the ventilated enclosure. Position and size of each vent are given in mm as shown in Figure 1.

Axial fan was fixed at inlet that can be operated at maximum 12 volts. Furthermore, honey comb structure was used to remove the flow disturbances as shown in Figure 2. Complete experimental setup is shown in Figure 3. Thermocouples were installed inside the enclosure and to the inner surface of heat source to record mean rise in surface and enclosure temperature.

5. Uncertainty and Results Validation

After calibration of sensors, each experiment was repeated thrice to ensure the repeatability and to calculate the standard deviation. Maximum deviation in temperature measurement was ± 0.5 °C due to the least count of temperature measuring system. Additionally, maximum uncertainty in reporting dimensions i.e. heat source length, diameter and thermocouple locations is ± 2 mm. Experimental results are reported with 97% precision and average standard deviation of results from reported value is 1.14%. Before starting experiments, heat source was placed in air quiescent medium and results were compared with Al-Arabi and Khamis data [15]. Results were found satisfactory as maximum percentage difference was less than 5%.

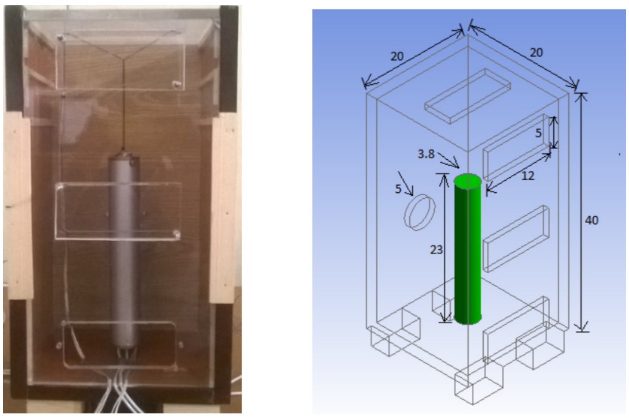

Figure 1. Manufactured and CAD model (left to right) of ventilated enclosure with dimensions (in mm)

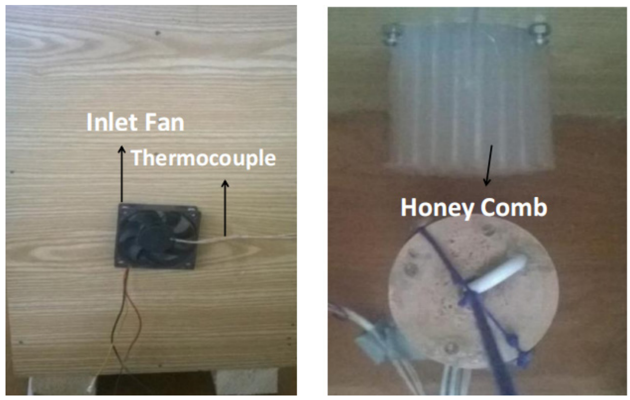

Figure 2. Inlet of ventilated enclosure (fan, honeycomb structure)

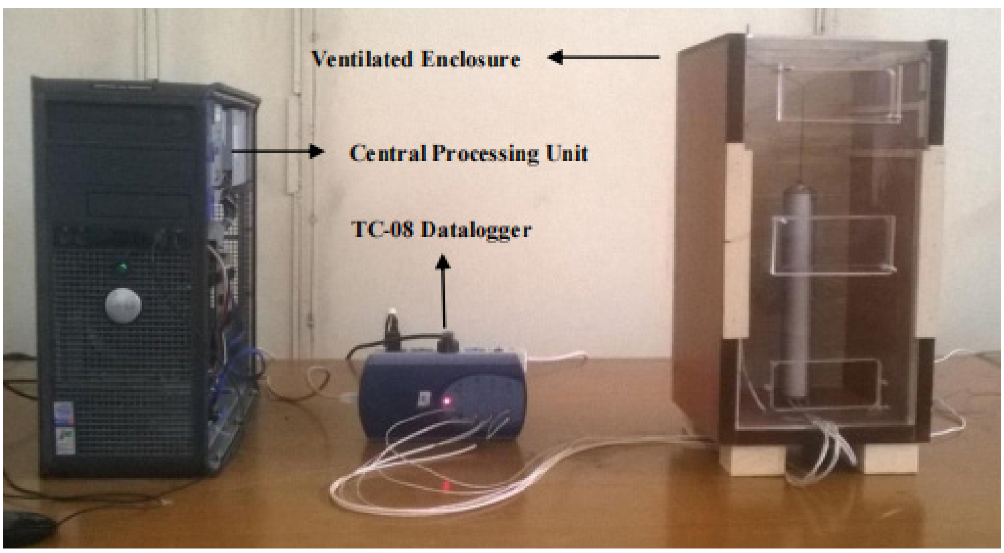

Figure 3. Experimental setup to study heat transfer inside the ventilated enclosure

6. Method and Measurements

After validation, heat source was hanged at the centre of the ventilated enclosure and operated at constant heat flux value while fan was operated at constant velocity. System took almost one hour to reach steady state. After reaching steady state, temperatures were recorded with the help of miniature K-type thermocouples and TC-08 data logger. Average heat transfer coefficient on the surface of heat source in various conditions was calculated through energy balance equations.

Total thirty five experiments were performed for the range of convective heat flux 236.76 w/m^2 to 976.08 w/m^2.

7. Results and Discussion

Effect of outlet area, height, position and fluid inlet velocity on convection heat transfer from the thin cylindrical heat source operated at various heat flux values inside the ventilated enclosure are discussed below.

8. Effect of Outlet Height, Area and Position

In order to study the effect of outlet height, three different outlet heights were used such as 45 mm (outlet:3), 200 mm (outlet:2) and 355 mm (outlet:1). Results were plotted in the form of average Nusselt number against the Richardson number as shown in Figure 4. It was observed that variation of outlet height at the front wall did not affect heat transfer in forced convection region. However, Nusselt number increased to 5% by changing the outlet position from front to the top wall as shown in Figure 5. This is because of placing the outlet at top wall of ventilated enclosure is assisting the natural convection flow.

By reducing the outlet area to 50%, Nusselt number decreases to 5% as shown in Figure 6. It was observed that volumetric flow rate of air increased by reducing the area but Nusselt number decreases due to resistance increment in the passage of air.

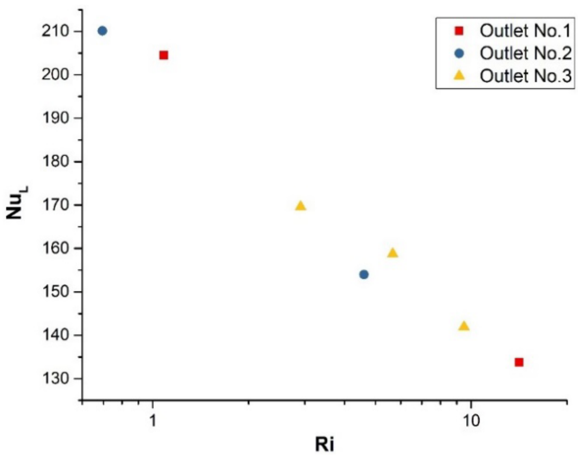

Figure 4. Effect of outlet height on convection heat transfer inside the ventilated enclosure having internal heating source

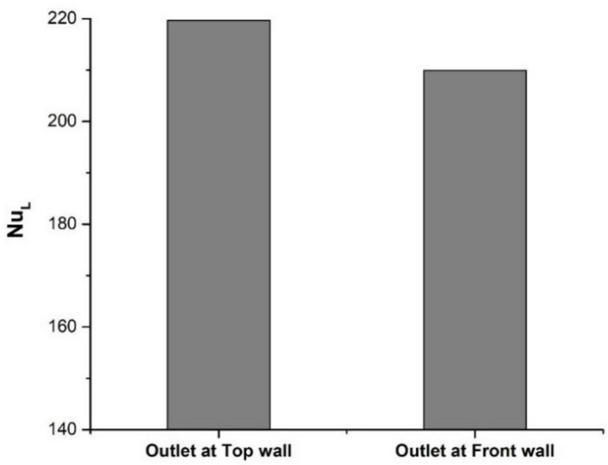

Figure 5. Effect of outlet position on convection heat transfer

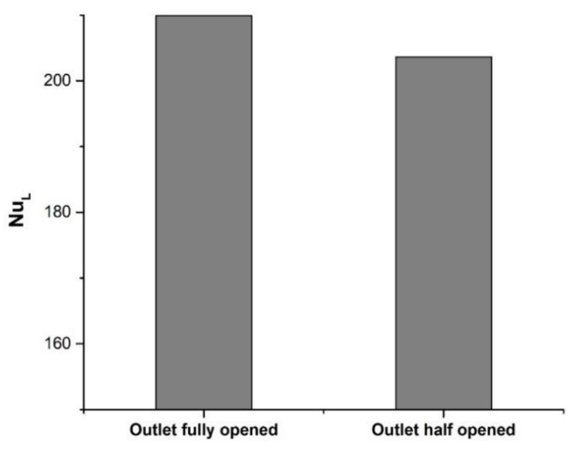

Figure 6. Effect of outlet area on convection heat transfer

9. Effect of Inlet Velocity

To study the effect of inlet velocity, heat source was operated at constant modified Grashof number i.e. 5.67E+09. Seven experiments were performed by varying velocity while outlet height, position, and heat flux were kept constant. It was observed that inlet velocity has a significant effect on convection heat transfer as shown in Figure 7. Figure 7 is divided into three sections i.e. forced, mixed and natural convection heat transfer. In mixed convection region, Nusselt number was varied from 120 to 160, but in forced convection there was a sharp increment in heat transfer and Nusselt number reached upto 216; while in natural convection region, Nusselt number suddenly decreased to 68. Trend of region "A" of Figure 7 was also observed in reference [16].

Maximum calculated heat losses were 4.1%. Almost one hour was required by the system to reach the steady state. Calculations showed that heat transfer coefficient was varied from 8.31 $w.m^{-2}.K^{-1}$ to 25.22 $w.m^{-2}.K^{-1}$ by changing inlet average velocity from 0 to 3.34 m/s.

10. Mean Rise in Temperature

Mean rise in surface temperature of cylindrical heat source and air temperature inside the ventilated enclosure was measured against the Richardson number as shown in Figure 8 and Figure 9. For this, heat source was operated at three different values of heat flux such as 237.42 w/m^2, 530.67 w/m^2 and 935.00 w/m^2. Mean rise in temperature inside the enclosure and on the surface of heat source is important variable to consider before designing of ventilated enclosure. From the constraint of maximum allowable temperature of heat source, one can approximate the required velocity of air.

To observe the variation of mean rise in temperature inside the ventilated enclosure, five thermocouples were used. Thermocouples were placed at the distance of 50 mm from side wall and at the height of 50 mm, 100 mm, 150 mm, 200 mm and 250 mm with the help of string. It was observed that in forced convection, mean rise in temperature inside the ventilated enclosure was almost uniform. While in natural convection, mean rise in temperature increased from bottom to the top of the enclosure as shown in Figure 10.

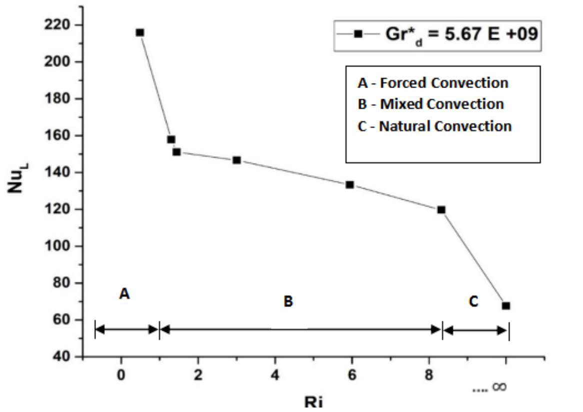

Figure 7. Effect of inlet velocity on convection heat transfer from cylindrical surface inside the ventilated enclosure

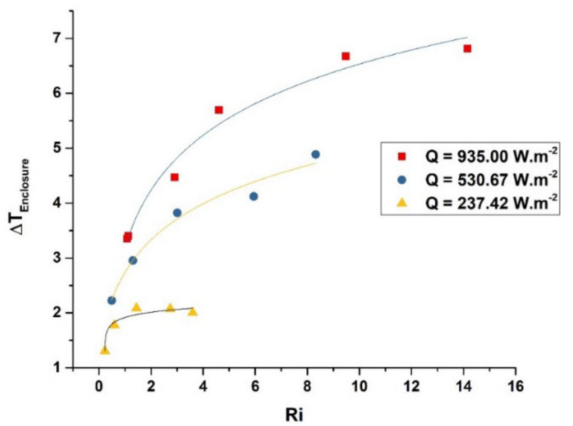

Figure 8. Mean rise in enclosure temperature for three different values of heat flux

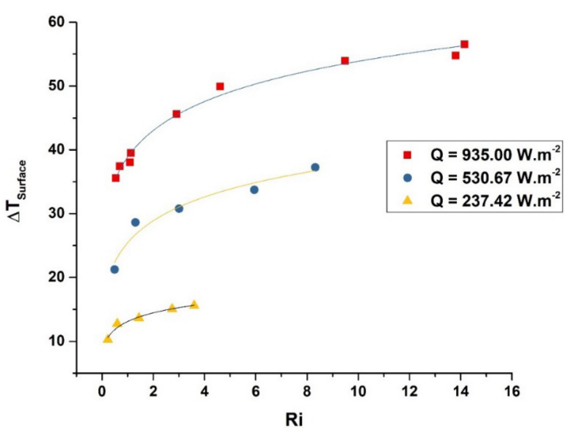

Figure 9. Mean rise in surface temperature of cylindrical heat source for three different values of heat flux

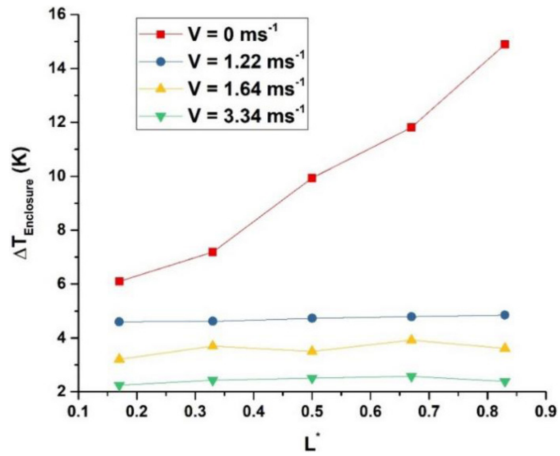

Figure 10. Variation of mean rise in temperature inside the air ventilated enclosure against the dimensionless height

11. Effect of Aspect Ratio

Aspect ratio (h/w) of ventilated enclosure was changed from 2 to 1.5 in order to study its effect on convection heat transfer. For this, two experiments were performed by operating inlet fan at 1.64 m/s and 0 m/s while heat source was operated at constant heat flux: 541.20 w/m^2. It was observed that surface temperature did not affect by changing aspect ratio, however mean rise in enclosure was affected by changing aspect ratio of enclosure under natural convection heat transfer as shown in Table 1. Heat transfer decreases by increase in aspect ratio, and same behaviour was observed by Vishnu C.S. and Anoop V. [17].

Table 1. Effect of aspect ratio on mean rise in temperature inside the enclosure

Convection Mode	Aspect Ratio = 2 $\Delta T_{Enclosure}$ (K)	Aspect Ratio = 1.5 $\Delta T_{Enclosure}$ (K)
Natural Convection	9.40	8.19
Forced Convection	3.82	3.62

12. Conclusions

Effect of axial fan velocity, aspect ratio of enclosure, outlet position, height and area on mixed convection is studied experimentally. It was observed that:

1) Average Nusselt number was increased from 68 to 216 by changing velocity from 0 to 3.34 m/s at constant modified Grashof number i.e. 5.67E+09.

2) Nusselt number decreased to 5% by changing the outlet position from top to the front wall or by 50% reduction in outlet area during forced convection.

3) Mean rise in temperature of enclosure increased from 8.19 K to 9.40 K by increasing aspect ratio of enclosure from 1.5 to 2 by operating heat source at constant heat flux i.e. 541.20 w/m^2.

Funding

This research was funded by Pakistan Institute of Engineering and Applied Sciences, Pakistan. It is hereby declared that authors have no conflict of interest of any kind.

Conflict of Interest

There is no conflict of interest.

Nomenclature

Gr^*	Modified Grashof number $Gr_L{}^* = \frac{g\beta L_c{}^4 q''}{k\nu^2}$
Nu_L	Average Nusselt number $Nu = \frac{hL_c}{k}$
Re	Reynold Number $Re = \frac{Inertia\,forces}{Viscous} = \frac{VL_c}{\nu} = \frac{\rho VL_c}{\mu}$
Ri	Richardson Number $Ri = \frac{Gr_L}{Re_L{}^2}$
Q_{total}	Total Heat Transfer $Q_{total} = Q_{in} = I \times V$
$Q_{convection}$	Convection Heat Transfer $Q_{convection} = h_{avg}\, A_s(T_{s,avg} - T_b)$
$Q_{radiated}$	Radiated Heat Transfer $Q_{radiated} = \varepsilon\, \sigma\, A_s\, (T_{s,avg}{}^4 - T_b{}^4)$
$Q_{conduction}$	Conduction Heat Transfer $Q_{conduction} = -kA\frac{dT}{dx}$
A_s	Surface Area
g	Gravitational acceleration
h	Convective heat transfer coefficient
I	Current
k	Thermal conductivity
L_c	Characteristic length
Pr	Prandtl number
Q	Heat source power
T_b	Ambient or bulk stream temperature
T_f	Film temperature
T_s	Surface temperature
V	Voltage
ρ	Density
μ	Dynamic viscosity
ε	Emissivity
υ	Kinematic viscosity

References

[1] Mangesh, D.S., Mahalle, A.M., 2013. Cooling of Electronic Equiments with Heat Sink: A review of Literature. IOSR Journal of Mechanical and Civil Engineering (IOSR-JMCE). 5(2), 56-61.

[2] Riaz, A., Ibrahim, A., Basit, A., et al., 2017. Numerical Simulation of Naturally Air Cooled Electronic Equipments Casing. International Bhurban Conference on Applied Sciences and Technology. DOI: https://doi.org/10.1109/IBCAST.2017.7868100

[3] Riaz, A., Basit, A., Ibrahim, A., et al., 2017. A Three-Dimensional CFD and Experimental Study to Optimize Naturally Air-Cooled Electronic Equipment Enclosure: Effects of Inlet Height, Heat Source Position and Buoyancy on Mean Rise In Temperature. Asia-pacific Journal of Chemical Engineering. 13(1). DOI: https://doi.org/10.1002/apj.2145

[4] Kusammanavar, B., Shashishekar, D., Seetharamu, D., 2012. Effects of Source Location on Natural Convection in a Square Cavity. International Journal of Engineering Research and Technology. 1(6).

[5] Chavan, S., Sathe, A., 2016. Natural Convection Cooling of Electronic Enclosure. International Journal of Trend in Research and Development. 3(4).

[6] Zaman, F.S., Turja, T.S., Molla, M.M., 2013. Byouyancy Driven Natural Convection Flow in an Enclosure with two Discrete Heatinf from Below. Procedia Engineering.

[7] Mariani, V., Coelho, L., 2007. Natural Convection Heat Transfer in Partially Open Enclosures Containing An Internal Local Heat Source. Brazilian Journal of Chemical Engineering. 24(3), 375-388.
DOI: https://doi.org/10.1590/S0104-66322007000300007

[8] Rocha, L.J.C., Souza, H.A., 2016. Numerical Study of the Influence of Internal Heat Source in Naturally Ventilated Offices. Mechanic and Energy. 69(1), 45-51.
DOI: https://doi.org/10.1590/0370-44672015690099

[9] Ishizuka, M., Nakagawa, S., 2008. Study on Natural Air Cooling Design of Electronic Equipment Casings: Effect of the Height and Size of Outlet Vent on the Flow Resistance. 2008 11th Intersociety Conference on Thermal and Thermomechanical Phenomena in Electronic Systems.

[10] Munoz, N.A.R., Palafox, J.F.H., Kohlhof, K., 2011. Numerical Study of Heat Transfer by Free and Forced Convection in a Ventilated Cavity. Sustainability in Energy and Buildings. 7, 91-99.
DOI: https://doi.org/10.1007/978-3-642-17387-5_10

[11] Ajmera, S.K., Mathur, A., 2015. Combined Free and Forced Convection in an Enclosure with Different Ventilation Arrangement. Procedia Engineering.
DOI: https://doi.org/10.1016/j.proeng.2015.11.456

[12] Mohammed, A.K., Talabani, Z.J., Ibraheem, R.R., 2013. Experimental Study of Steady State Natural Convection Heat Transfer From Cylindrical Heater in a Vented Enclosure. Journal of Science and Engineering. 2(2), 87-96.

[13] Ajmera, S.K., Mathur, A., 2015. Combined Free and Forced Conection in an Enclosure with Different Ventilation Arrangements. Procedia Engineering. 127, 1173-1180.
DOI: https://doi.org/10.1016/j.proeng.2015.11.456

[14] Bilgen, E., Muftuuoglu, A., 2008. Cooling Strategy by Mixed Convection of a Discrete Heater at its Optimum Position in a Square Cavity with Ventilation Ports. International Communications in Heat and Mass Transfer. 35(5), 545-550.
DOI: https://doi.org/10.1016/j.icheatmasstransfer.2008.01.001

[15] Al-Arabi, M., Khamis, M., 1982. Natural Convection Heat Transfer from Inclined Cylinders. International Journal of Heat & Mass Transfer. 25, 3-15.

[16] Riaz, A., Shah, A., Basit, A., et al., 2019. Experimental Study of Laminar Natural Convection Heat Trasnfer from Slender Circular Cylinder in Air Quiescent Medium. International Bhurban Conference on Applied Sciences & Technology.
DOI: https://doi.org/10.1109/IBCAST.2019.8667230

[17] Vishnu, C.S., Anoop, V., 2014. Convection Heat Transfer in a Vertical Vented Enclosure. International Journal of Mechanical Engineering and Information Technology. 2(9), 737-745.

Semiconductor Science and Information Devices
https://ojs.bilpublishing.com/index.php/ssid

ARTICLE

Experimentation on Optimal Configuration and Size of Thin Cylinders in Natural Convection

Ali Riaz[1] **Adnan Ibrahim**[2*] **Muhammad Sohail Bashir**[3] **Masroor Asghar**[4] **Muhammad Abdullah**[1] **Ajmal Shah**[1]

1. Department of Mechanical Engineering, Pakistan Institute of Engineering and Applied Sciences, Islamabad, 45650, Pakistan
2. School of Engineering Science, University of Science and Technology of China, Hefei, 230027, China
3. Hefei National Laboratory for Physical Sciences at the Microscale, CAS Key Laboratory of Soft Matter Chemistry, Department of Polymer Science and Engineering, University of Science and Technology of China, Hefei, Anhui, 230026, China.
4. Department of Information Technology, University of Southern Queensland, Toowoomba, 4350, Queensland, Australia

ARTICLE INFO

Article history
Received:16 May 2022
Revised: 16 June 2022
Accepted: 24 June 2022
Published Online: 4 August 2022

Keywords:
Natural convection
Thin cylinders
Flat plate
Nusselt number

ABSTRACT

In this paper, an experimental study of laminar, steady state natural convection heat transfer from heated thin cylinders in an infinite air medium has been reported. Two electrically heated cylinders having the same slenderness ratio (L/D) i.e. 6.1 but different diameters i.e. 3.8 cm and 5.08 cm were used. 105 experiments were carried out to study the effect of diameter and inclination angle of thin cylinder on natural convection heat transfer. After mandatory corrections of radiation and endcap heat losses, convective heat transfer results were presented in the form of local and average dimensionless numbers. For vertical configuration of thin cylinder, Nusselt number was varied from 52.99 to 95.10 corresponding to $1.28\times10^{8}\leq Ra^{*}_{L}\leq1.08\times10^{10}$. While for horizontal configuration, Nusselt number was varied from 10.74 to 17.78 corresponding to $9.42\times10^{4}\leq Ra^{*}_{D}\leq8.17\times10^{6}$. Results were compared with the published data and found satisfactory as the maximum percentage difference was only 3.09%. The essence of research is that the heat transfer coefficient increases with decrease in diameter and increase in inclination angle. Smoke flow visualization was done to capture patterns of fluid flow. Finally, comparison was made to quantify increase in Nusselt number from slender cylinder as compared to the flat plate.

*Corresponding Author:
Adnan Ibrahim,
School of Engineering Science, University of Science and Technology of China, Hefei 230027, China;
Email: adnan36@mail.ustc.edu.cn

DOI: https://doi.org/10.30564/ssid.v4i2.4720

Copyright © 2022 by the author(s). Published by Bilingual Publishing Co. This is an open access article under the Creative Commons Attribution-NonCommercial 4.0 International (CC BY-NC 4.0) License. (https://creativecommons.org/licenses/by-nc/4.0/).

1. Introduction

Heat transfer from slender (thin) cylindrical surfaces through natural convection has broad spectrum in engineering applications such as fuel rods of nuclear power plant, cylindrical tubes of steam generator and car radiator, electrical resistive heating components, nuclear reactor insulation design and many others. Slender cylinders are different from thick cylinders because in thin cylinders, thermal boundary layer thickness is comparable to the radius of the cylinder [1]. This characteristic effect heat transfer greatly. Popiel [2] correlated the data of Cebeci [3] in order to establish the criteria of thick and thin cylinder for isothermal vertical cylinders in laminar region as shown in Equation (1). It is valid for the range of Prandtl number from 0.01 to 100.

$$Gr_H^{0.25}\frac{D}{H} \leq 11.474 + \frac{48.92}{Pr^{0.5}} - \frac{0.006085}{Pr^2} \quad (1)$$

On the basis of orientation, thin cylinders can be divided into horizontal and vertical configuration. Available literature in this regard is mentioned below in a brief manner.

1.1 Thin Cylinders in Vertical Position

Vertical flat plate correlations are applicable to the vertical thick cylinders of length ‘L’ and diameter ‘D’, if they are fulfilled the condition given in Equation (2) [4].

$$\frac{D}{L} \geq \frac{35}{Gr_L{}^{1/4}} \quad (2)$$

Churchill and Chu [5], Patrick H. Oosthuizen and Jane T. Paul [6,7], correlations are available for different boundary conditions and configurations of vertical flat plate. For thin cylinders, correlations depends upon slenderness ratio (L/D) to incorporate curvature effects. In this regard, widely used theoretical, numerical and experimental correlations are stated below.

Sparrow and Gregg [8] presented first analytical solution for the laminar natural convection flow over the surface of vertical cylinder. They assumed cylindrical surface at constant temperature and solved conservation equations by applying similarity method and power series expansion. C.O Popiel et al. [2] gave a correlation by performing transient analysis (Lumped capacitance method because Biot number was less than 0.01) to calculate average convective heat transfer coefficient. Experiments were performed on isothermal vertical slender cylinder for the Rayleigh number 1.5×10^8 to 1.1×10^9 and dimensionless height $0 \leq H/D \leq 60$ in an infinite air medium.

Yang [9] performed experiments by keeping q_w *and* T_w constant respectively and derive empirical correlations. These correlations are valid for all fluids ($0 \leq Pr \leq \infty$) and for $R_{aH} < 10^9$. Al-Arabi and Khamis [10] published empirical correlation for isothermal cylinder surrounded by air to approximate average Nusselt number in laminar and turbulent region. Ali Riaz et al. [11] experimentally determined local variation of heat transfer coefficient across the length of cylinder placed in infinite air medium.

1.2 Horizontal Heated Thin Cylinder

Limited coorelations are available in horizontal configuration as compated to vertical. Nusselt [12] solved equation analytically to determine the heat transfer coefficients for the horizontal cylinders in air or liquids for $10^4 \leq Gr_D Pr \leq 10^8$. Morgan [13] correlated the results of Koch for the range: $4\times10^3 \leq Gr_D Pr \leq 6\times10^6$. Dyer [14] proposed correlation for iso-flux horizontal cylinder for the range: $10^3 \leq Gr_D^* Pr \leq 10^{10}$.

1.3 Inclined Heated Thin Cylinder

Al-Arabi and Khamis [10] studied natural convection heat transfer from inclined thermal cylinders in detail. They plotted results in local and average dimensionless form inside the laminar and turbulent region. P.H. Oosthuizen and V. Mansingh [15] investigated natural and forced convection heat transfer from short inclined cylinders having length to diameter ratio between 1.5 and 16.

By examining research studies, it is observed that prime focus of research was on vertical and horizontal configuration of heated thin cylinders in infinite air medium. Limited studies regarding iso-flux boundary condition on thin cylindrical element have been reported as compared to isothermal condition. Experimental results describing the effect of inclination on natural convection heat transfer is also limited. In this regard, only Al-Alarabi M. and Y. Salman [16] and P.H. Oosthuizen and V. Mansingh [15] experimental data are available, to the best knowledge of the authors. This was motivation behind this study.

In this research, experimental approach was used to generate benchmark data regarding thermal performance of thin cylinders in various configurations such as 0°, 30°, 45°, 60° and 90° inside the infinite air medium. Furthermore, experiments were conducted to analyze the effect of cylinder diameter on natural convection heat transfer.

During literature review, considerable difference in data regarding average Nusselt number over the surface of vertical cylinder by various researchers was observed [2,3,9,10]. The empirical correlations of heat transfer coefficient show a widespread and some percentage of error. Therefore, a large number of experiments were conducted to suggest which correlation is more appropriate in predicting results in stated range. At the end, results are reported in dimensionless form. This data can be used to perform numerical simulations and to formulate an empirical correlation of heat transfer.

2. Energy Balance

Heat supply to thin cylinders must be equal to radiation and natural convection heat transfer from the surface to ambient air plus heat losses through end caps as shown in Figure 1 and written in the form of Equations (3) to (8).

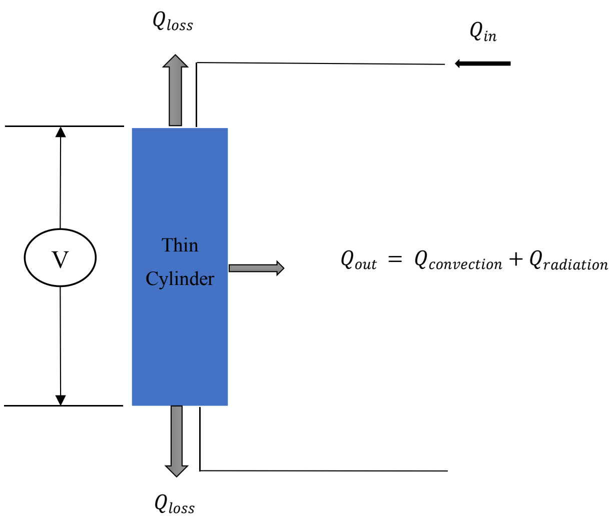

Figure 1. Energy balance on schematic view of heat source

$$Q_{total} = Q_{in} = Q_{convection} + Q_{radiation} + Q_{conduction} \tag{3}$$

$$Q_{in} = I \times V = Q_{total} = h_{combine}\, A_s(T_s - T_b) + Q_{loss} \tag{4}$$

where, $h_{combine} = h_{convective} + h_{radiative}$ (5)

$$Q_{loss} = Q_{conduction-end\ caps} + Q_{radiation-heat\ source} \tag{6}$$

As it is steady state experimental study, so mathematically it can be written as:

$$Q_{in} = Q_{out} \tag{7}$$

Fourier law of heat conduction has been used to calculate conduction heat losses. It is given as [17]:

$$Q = -kA\frac{dT}{dx} \tag{8}$$

Heat losses in the form of radiation were calculated through Equation (9) [11].

$$Q_{radiated} = \varepsilon\, \sigma\, A_s\, ({T_{s,avg}}^4 - {T_b}^4) \tag{9}$$

Convective or radiative heat transfer coefficient can be calculated through Newton law of cooling written in Equation (10) [18].

$$Q_{convection/radiation} = h_{conv.\,rad}\, A_s(T_{s,avg} - T_b) \tag{10}$$

Physical properties of air have been calculated through following relation [19]:

$$PP = A + BT_f + C{T_f}^2 + D{T_f}^3 \tag{11}$$

where, A, B, C and D are the thermodynamics constants and are stated in Table 1. T_f is the film temperature, while 'PP' stands for physical properties such as C_p , μ, k and ρ.

Table 1. Thermodynamic constants for physical properties of air

Thermodynamic \ Constants	A	B	C
Specific Heat (C_p) - J/Kg K	1024.06	–0.175768	3.70976 × 10^{-4}
Viscosity (μ) - (Kg/m.sec)	2.12075 × 10^{-6}	6.24755 × 10^{-8}	–2.6162 × 10^{-11}
Thermal Conductivity (k) (W/m. K)	2.317 × 10^{-3}	8.7113 × 10^{-5}	–2.55188 × 10^{-8}

Density was calculated through ideal gas law and thermal expansion coefficient was approximated through reciprocal of absolute film temperature. All physical properties were calculated at average film temperature: $T_{f,avg}=(T_{s,avg}+T_b)/2$. Average heat transfer coefficient for vertical configuration has been calculated as,

$$\overline{h_L} = \frac{\sum_{i=1}^{3} h_{xi}\Delta x_i}{L} \tag{12}$$

where x_i is the distance from the bottom of heat source. For horizontal configuration, it can be calculated as,

$$\overline{h_L} = \frac{\sum_{i=1}^{3} h_{xi}\Delta c_i}{2\pi r} \tag{13}$$

where 'c_i' is the circumference distance while 'r' is the radius of cylinder.

Average Nusselt number has been calculated as,

$$Nu = \frac{\overline{h_L} \times L}{k} \tag{14}$$

As it is constant heat flux case, so average modified Grashof number and modified Rayleigh number has been calculated as follows:

$$Gr_L{}^* = \frac{g\beta L^4 q''}{k\nu^2} \tag{15}$$

$$Ra_L{}^* = Gr_L{}^*.Pr \tag{16}$$

'L' should be replaced with 'D' in above relations for horizontal configuration. Precision of experimental data was stated after calculating standard deviation as shown in Equation (17), where, $\bar{x}$ is the mean value and 'n' is the total number of terms.

$$SD = \sqrt{\sum |x - \bar{x}|^2 / n} \quad (17)$$

3. Experimental Setup

This section comprises on designing and manufacturing of thin cylinders along with wooden enclosure to provide undisturbed environment for natural convection study.

3.1 Designing

Designing of thin cylinders comprises on determining its diameter and length or L/D ratio. Depending upon scope of research study such as laminar; the length and diameter were selected. As one of the objectives of present study was to study the effect of thin cylinders diameter on natural convection in laminar region, so two different commercially available diameters were selected such as 3.8 cm and 5.08 cm. By considering range of present study i.e. $2.77\times10^{8} \leq Ra^{*}_{L} \leq 1.08 \times 10^{10}$ (laminar region), 31 cm length of cylinder was calculated. Designed range of modified Rayleigh number was achieved for designed length and diameter of cylinder through single phase power supply by varying heat flux from 9.39 $w.m^{-2}$ to 638.99 $w.m^{-2}$.

3.2 Manufacturing and Fabrication

Heating rod having maximum 1000 watts power rating was placed at center of cylindrical casing having 5.08 cm diameter and 31 cm length. To control heat losses from ends, Perspex disk having 5 cm diameter and 1.27 cm thickness was used because of its low thermal conductivity. Center hole of 5 mm diameter was drilled at the Perspex disk to provide an electrical connection. Silica gel was used to completely seal the cylinders from fresh air. Manufactured thin cylinder with electric connections and attached thermocouples is shown in Figure 2. On a similar basis, another thin cylinder having 3.8 cm diameter and 23 cm length was manufactured.

Figure 2. Aluminum thin cylinder having five thermocouples at the inner surface

After manufacturing thin cylinders of aforementioned dimensions, recorded maximum temperature difference was 74.24 K corresponding to 638.99 $w.m^{-2}$ convective heat flux value. Thus, through proper designing, temperature of thin cylinders can be controlled and research can be performed for designed range of modified Rayleigh number.

As rising plume in natural convection is sensitive to the outer disturbances so wooden enclosure was manufactured having front transparent wall made up of Perspex for natural convection study and smoke flow visualization. Complete experimental setup is shown in Figure 3.

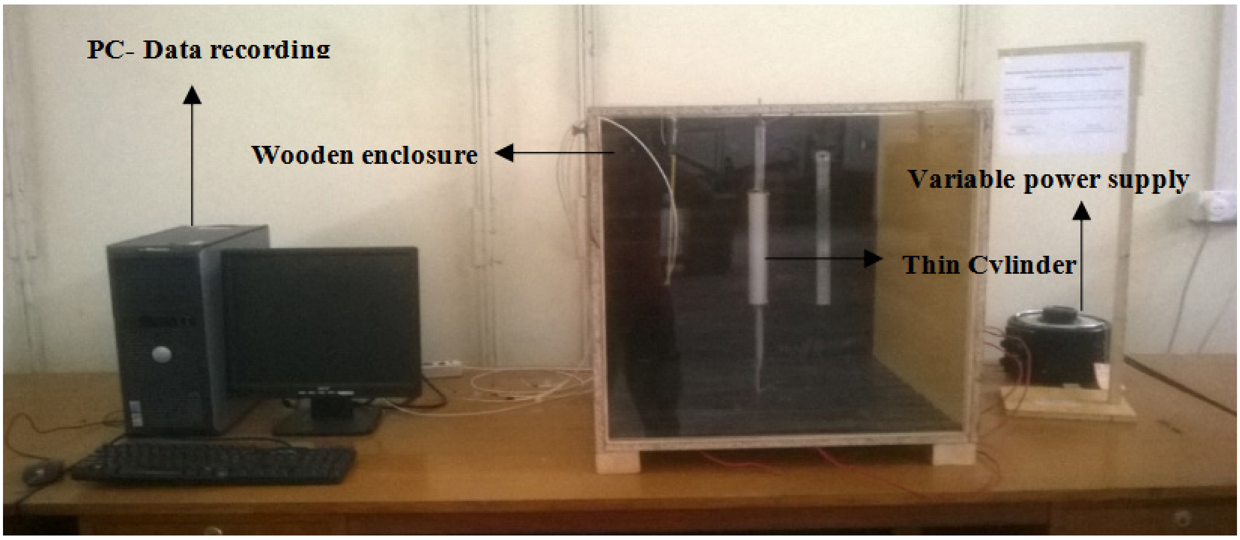

Figure 3. Experimental setup having enclosure for infinite medium

3.3 Method and Measurements

Generally, in experimentation sensors disturb the field and thus affect the measurement. Therefore, special attention should be taken to attach thermocouples to the surface so that they attain the surface temperature rather than perturbed temperature. Thermocouple installation is one of the main tasks as briefly described below:

H. Shaukatullah and A. Claassen [20] claimed that the best method of thermocouple attachment is through thermal conductive epoxy. Additionally, they reported that k-type thermocouples are better than T-type because of their lower equivalent thermal conductivity. Therefore, miniature k-type thermocouples were attached with thermal conductive epoxy to the inner surface of thin cylinder so that it cannot disturb the external thermal and hydrodynamic boundary layer. Three thermocouples were attached at the inner surface of the cylinder. Their positions at the surface of cylinder are shown in Figure 4. All dimensions are in centimeters. Figure 4 also shows the cross-sectional view of thin cylinder i.e. Nichrome wire, air gap, Aluminum sheath and Perspex end caps. Ambient temperature was measured by placing thermocouple at axially 15 cm away from the bottom of the thin cylinder inside the enclosure.

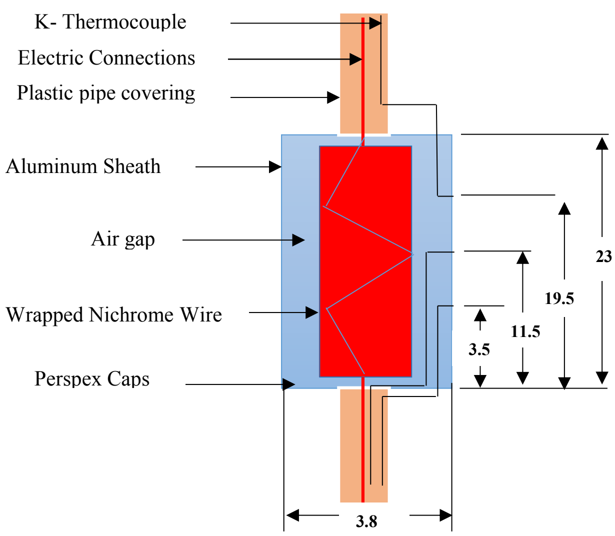

Figure 4. Schematic view of thin cylinder. All dimensions are in cm.

Variable power supply was used in experiments to supply variable voltages in order to perform experiments at various convective heat flux values. Upon reaching steady state, surface temperature values were recorded for fifty seconds with the help of TC-08 datalogger, and then average surface temperature was calculated. Steady state is defined as the state at which temperature change is smaller than ± 0.1 °C in a 2 min period [21]. All experiments were performed in an isolated and quiescent room by turning off the blowers and fans of the laboratory and it took almost two hours to reach steady state.

105 experiments were performed to completely expedite the problem. On average, calculated heat loss was 6.5% of the total heat flux. Seven experiments were performed for each thin cylinder configuration and diameter to calculate heat transfer coefficient for the designed range of modified Rayleigh number. Each experiment was repeated thrice to ensure repeatability and to measure standard deviation. This study is divided into four cases:

3.3.1 Case: A

Thin cylinder having 23 cm length and 3.8 cm diameter was hanged in a vertical position. Total seven experiments were performed for the range of convective heat flux 14.17 $w.m^{-2}$ to the 515.22 $w.m^{-2}$. Maximum temperature difference observed corresponding to the range of aforementioned convective heat flux was 49.27 K.

3.3.2 Case: B

Thin cylinder having 31 cm length and 5.08 cm diameter was vertically hanged. Seven experiments were performed for the range of convective heat flux 9.39 $w.m^{-2}$ to 638.99 $w.m^{-2}$. Maximum average temperature difference recorded during experimentation was 74.24 K.

3.3.3 Case: C

Thin cylinder having 3.8 cm diameter was fixed in a horizontal position with the help of fixture. Total seven experiments were performed for the range of convective heat flux 14.33 $w.m^{-2}$ to 517.78$w.m^{-2}$; 45.64 K was the maximum measured temperature difference. Three thermocouples were attached along the length of the cylinder. Thin cylinder was rotated along its axis to measure the circumferential variation in temperature. The maximum variation of temperature measured from thermocouples in the above mentioned range of heat flux was less than 1 °C along the length and circumference of the cylinder. Range of convective average heat transfer coefficient for the horizontal thin cylinder configuration is 7.54 w.m.$^{-2}$. k^{-1} to 11.42 w.m.$^{-2}$. k^{-1} for the range of convective heat flux from 13.33 $w.m^{-2}$ to 517.78 $w.m^{-2}$.

3.3.4 Case: D

Thin cylinder having 31 cm length and 5.08 cm diameter was placed in a horizontal position with the help of a fixture. Maximum average temperature difference recorded during experimentation was 76.08 K. Six thermocouples were attached to the inner surface of the thin cylinder. It was observed that when thin cylinder in horizontal orientation, the temperature varied only in circumferential direction not in axial. Calculations showed that maximum thermal losses were 8.06% of the total heat flux. Range of convective heat transfer coefficient was from 3.81 $w.m^{-2}. K^{-1}$ to 10.89 $w.m^{-2}. K^{-1}$ corresponding to the range of heat flux from 9.31 $w.m^{-2}$ to the 643.11 $w.m^{-2}$.

4. Results and Discussions

Comparison of results with the already published results is a necessary step in order to validate experimental data. Validation confirms the authenticity of the research and helps to obtain reliable results. For validation, initial experiment was performed and results were compared with the already published results of Alarabi and Khamis [10]. Alarabi and Khamis performed experiment on thin cylindershaving 50.8 mm diameter and 30 cm length and the temperature difference between ambient and surface temperature was 70 ± 4 °C. Thin cylinder having same dimensions was manufactured and similar experimental settings were achieved in the laboratory for comparison of experimental results. Comparison of results in the form of average heat transfer coefficient and Nusselt number are shown in Table 2.

Table 2. Comparison of experimental data with Alarabi and Khamis [10]

Source	Nu_L
Al Arbi and Khamis [10]	102.41
Present Study	99.24
Precentage Difference	3.09 %

Temperature variation in Alarabi experiment was ± 4 °C and they did not clearly mention the ambient and surface temperature. One can obtain the same temperature difference i.e. 70 °C through number of ambient and surface temperature values. This ambiguity yields into different film temperature which resulted into different physical properties of fluid. This may be a reason of difference between the present and Al Arabi and Khamis experimental results. At last, least count and sensitivity of the sensors used in experimental study may also contribute to the error. In the light of above discussion, one can confidently say that present experimental results are in good agreement with the published results. Surface and ambient temperature of the first experiment of case: A is shown in Figure 5. After achieving steady state, temperature was recorded at interval of one second for fifty seconds with the help of datalogger.

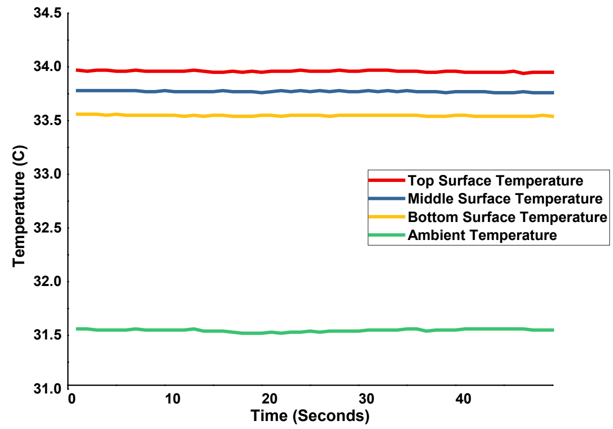

Figure 5. Steady state temperature at 14.17 $W.m^{-2}$ (Case: A)

Temperature difference between ambient and average surface value at various heat fluxes for thin cylinders of case A and B is shown in Figure 6. At the same heat flux value, the temperature difference was higher for case B as compared to case A. This is because of functional dependency of heat transfer coefficient on physical parameter of thin cylinder such as diameter. As the diameter decreases the heat transfer coefficient increases and temperature difference reduces. Furthermore, one can easily observe that temperature increment with convective heat flux is almost linear in both cases, the difference lies in slope of the line. Average Nusselt number as a function of convective heat flux is shown in Figure 7.

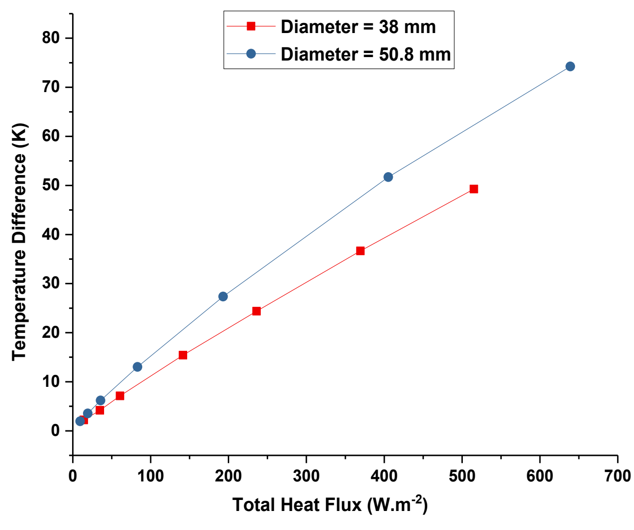

Figure 6. Temperature difference versus total heat flux

Variation of average Nusselt number as a function of modified Rayleigh number - calculated through convective heat flux – for vertical and horizontal configuration of thin cylinder is presented in semi log graph as shown in Figure 8 and Figure 9 respectively. Logarithmic increment in average Nusselt number with modified Rayleigh number can be observed from both figures. Range studied for vertical configuration is $1.28 \times 18^{8} \leq Ra^{*}_{H} \leq 1.08 \times 10^{10}$ while for horizontal configuration the range is $1.99 \times 18^{5} \leq Ra^{*}_{D} \leq 8.15 \times 10^{6}$.

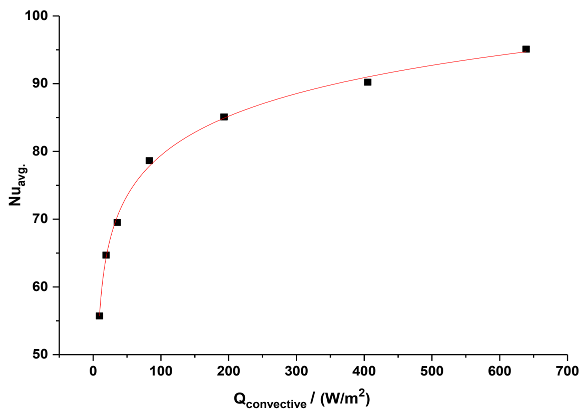

Figure 7. Variation of average Nusselt number with convective heat flux

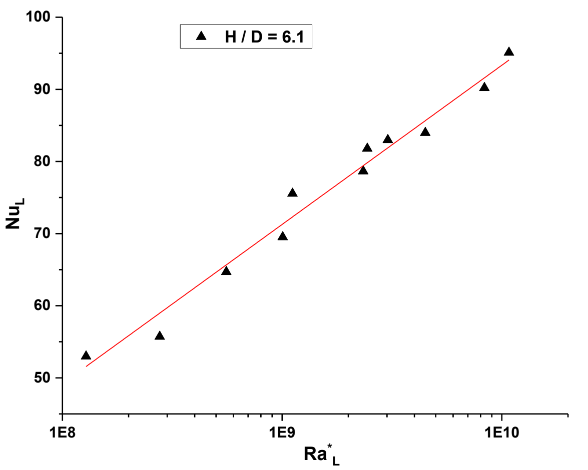

Figure 8. Average Nusselt number as a function of modified Rayleigh number in vertical configuration

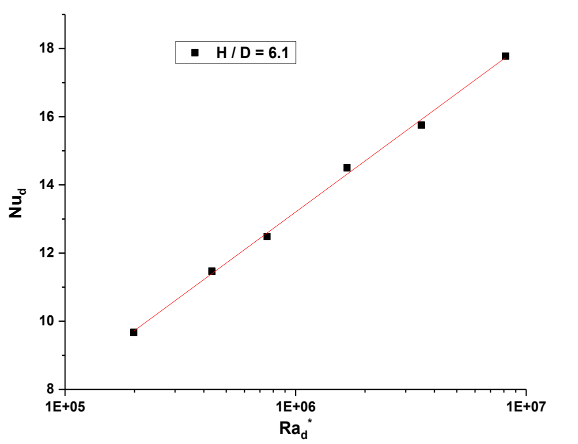

Figure 9. Average Nusselt number as a function of modified Rayleigh number in horizontal configuration

Design and experimental parameters ranges are reported in Table 3.

Table 3. Critical design and experimental parameters

S. No.	Parameters	Values
1	Diameter of thin cylinders	3.8 cm, 5.08 cm
2	Length of thin cylinders	31 cm
3	Heat flux range	9.39 to 638.99 $W.m^{-2}$
4	Max. temperature difference	74.24 K
5	Modified Rayleigh number range for vertical configuration	2.77×10^{8} to 1.08×10^{10}
6	Nusselt number range for vertical configuration	52 to 95
7	Modified Rayleigh number range for horizontal configuration	1.8×10^{5} to 1.9×10^{7}
8	Nusselt number range for horizontal configuration	9.6 to 18

4.1 Effect of Thin Cylinder Diameter

Nusselt number on the surface of thin cylinder is functionally dependent on length to diameter ratio, and the Rayleigh number (for of isothermal case) or modified Rayleigh number (for iso-flux case). Diameter of thin cylinderis the prime parameter that significantly affects the natural convection heat transfer phenomena. Heat transfer coefficient varies significantly from heated flat plate (Diameter $\rightarrow\infty$) to the slender cylinder having few millimetres diameter. One of the main objectives of this research was to experimentally examine the effect of thin cylinder diameter, therefore, 38 mm and 50.8 mm diameter were used.

As the length of the two thin cylinders was different so heat transfer coefficient was compared against the same Rayleigh number. It was observed that heat transfer coefficient varied decisively by changing the diameter as shown in Figure 10. From graph, it is obvious that as diameter decreases the average heat transfer convective coefficient increases. It can also be observed that the maximum increment in heat transfer coefficient decreases as Rayleigh number increases. This observation shows that diameter has more pronounced effect in laminar region as compared to the turbulent region.

At modified Rayleigh number 3.05E+08, the increase in heat transfer coefficient from 5.08 cm diameter to 3.8 cm diameter was 41.86% while this increment reduced to 31.43% at 2.44E+09 modified Rayleigh number. As the diameter decreases the curvature effect becomes more significant and affecting the development of thermal boundary layer which results into an increment in heat transfer coefficient. The same trend was also observed by Fumiyoshi KIMURA et al. [22] and Al Arabi and Khamis [10]. This is primarily due to thinning of thermal boundary layer around the cylinder.

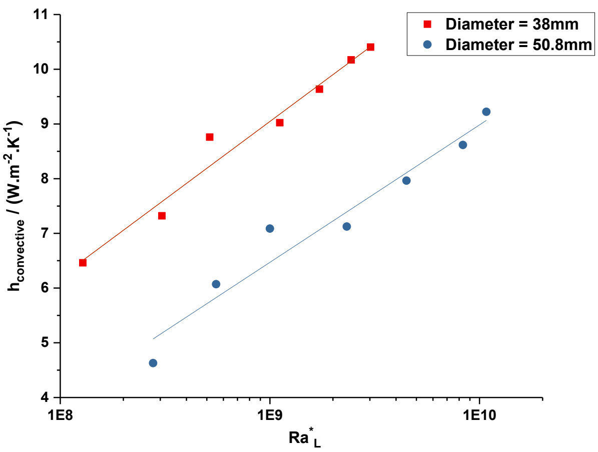

Figure 10. Heat transfer coefficient as a function of Rayleigh and diameter having same H/D ratio

Combined (convective and radiative) heat transfer coefficient was calculated by not subtracting the radiation heat losses from the total heat flux. The variation of combined heat transfer coefficient at various total heat flux values for two different diameter thin cylinders having same H/D ratio is shown collectively in Figure 11. Logarithmic trend was observed in plotted values of Figure 11.

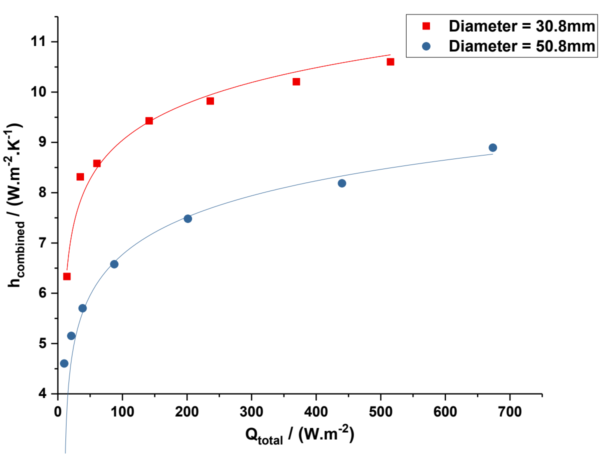

Figure 11. Combined heat transfer coefficient as a function of diameter and total heat flux

4.2 Effect of Thin Cylinders Inclination

Variation of average heat transfer coefficient with inclination angle - measured from vertical axis - is shown in Figure 12 and Figure 13 respectively. Both figures depicted that at same heat flux level, heat transfer coefficient increases with increase in inclination angle. It can also be observed that heat transfer increases with increment in Grashof number. Rise in heat transfer coefficient was more profound from 0° to 45° as compared to 45° to 90° inclination of cylinders. Same trend was observed by Al-Arabi and Y. Salman [16] and P.H. Oosthuizen and Mansingh, Vivek [15]. Development of thermal boundary layer in various configuration is the reason behind this experimentally observed trend as shown in smoke flow visualization section. In horizontal configuration, thickness of thermal boundary increases as one traversed from bottom to upward. This results in decrement of heat transfer coefficient.

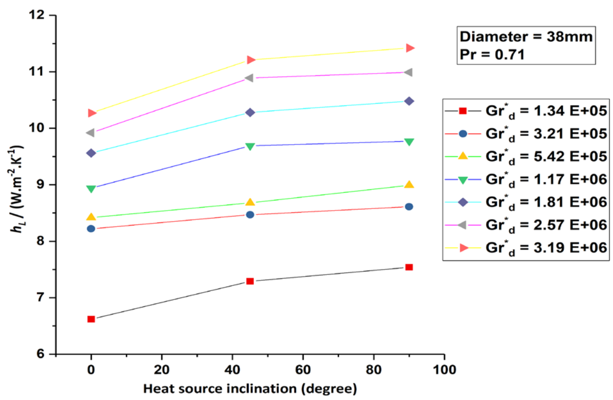

Figure 12. Variation of average heat transfer coefficient versus inclination angle of 3.8 cm diameter of thin cylinder

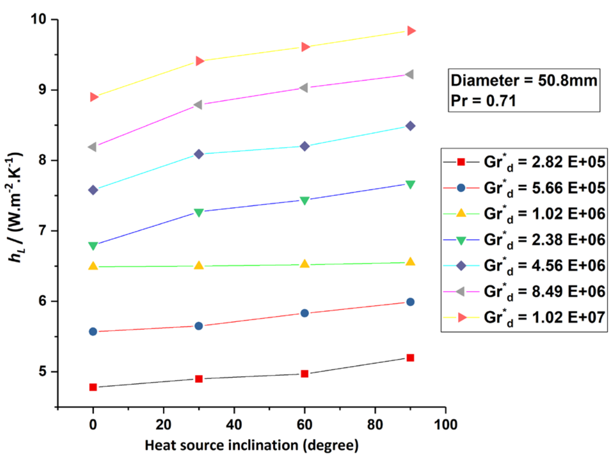

Figure 13. Variation of average heat transfer coefficient versus inclination angle of 5.08 cm diameter of thin cylinder

4.3 Uncertainty Analysis

Maximum uncertainty in temperature measurement is ± 0.5 °C calculated by comparing with mercury digital thermometer. This is mainly due to the least count of temperature measuring system i.e. thermocouple and datalogger. Although to minimize temperature measurement error to much extent a calibration process was done but experimentally one cannot achieve 100% accuracy due to limitations in sensors. Additionally, maximum uncertainty in reporting dimensions i.e. thin cylinder length, diameter and thermocouple locations is ± 2 mm. Uncertainty in results was calculated by performing each experiment thrice. Experimental results are reported with 96.8% precision and average standard deviation from reported value is 1.61%.

4.4 Smoke Flow Visualization

Pakistani burning incense stick was used for the visualization of smoke flow. This exercise was done just for the sake of visualization of streamlines inside the laminar thermal boundary layer at different configurations. Temperature was recorded at steady state and then smoke flow pattern was captured.

Axial flow pattern was observed at the surface of vertical configuration of thin cylinder while cross flow pattern was observed in horizontal configuration. It can be seen from Figure 14 that smoke flow was thinner at the bottom and thicker at the top. Cross and axial flow pattern were observed in inclined (45°) configuration as shown in Figure 15. From Figure 16, it can be easily observed that how hot plume raised in a laminar fashion till the end of the cylinder, which is also supported by the experimental data as the Rayleigh number is 8.03E+06 (laminar region).

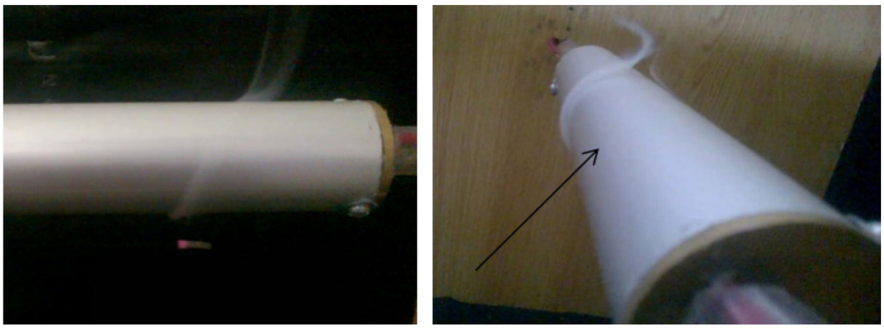

Figure 14. Smoke flow visualization at Ra^*_D=1.88E+06

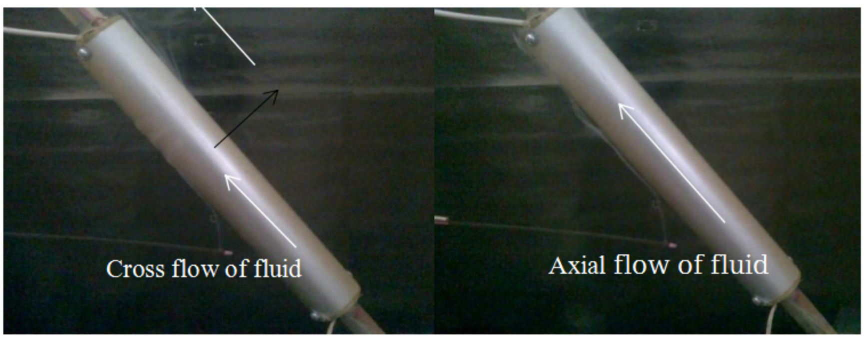

Figure 15. Smoke flow visualization at Ra^*_L=2.89E+09

Figure 16. Smoke flow visualization at Ra^*_L=5.07E+08

5. Validation of Results

Experimental results are validated after comparing with published data. Comparison of present data with theoretical data of H.R. Lee et al. [22] and experimental results of S. Jarall and A. Campo [23] is shown in Figure 17. Ratio of Nusselt number of cylinder to flat plate was plotted against a dimensionless parameter 'λ'. Correlation equation by Raithby and Hollands [24] was used to calculate local Nusselt number at vertical flat plate. This comparison also validated the present study as results are in between the published experimental and theoretical results. However present results are slightly higher than the theoretical results; this may be because of disturbance caused by sensors during measurement.

Average surface temperature was assumed over the whole cylindrical surface in order to make comparison with Al-Arabi and Khamis correlation [10] as it was proposed for isothermal case. Present results are highly in agreement with the published data as shown in Figure 18. It was also observed that Al-Arabi and Khamis correlation can be used with confidence for: $1.28 \times 10^8 \leq Ra^*_L \leq 1.08 \times 10^{10}$.This exercise assured that Al-Arabi and khamis results are more credible than other mentioned correlations under the sub-heading of 'vertical thin cylinder'.

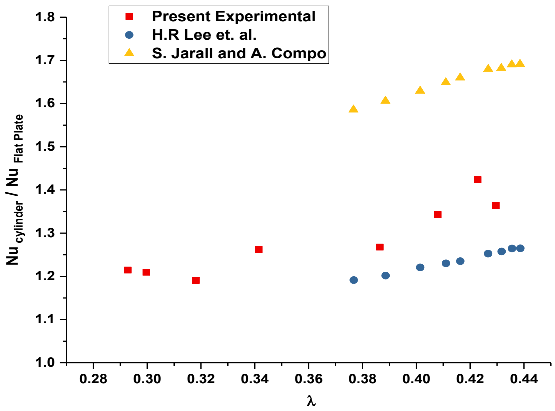

Figure 17. Comparison of present experimental results with H.R. Lee et al. published data

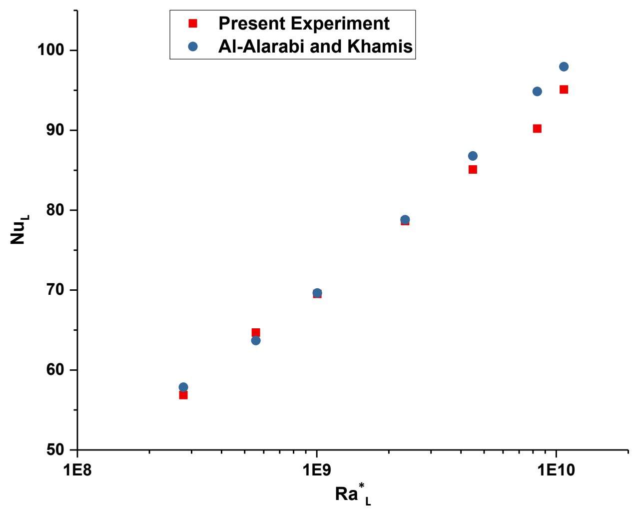

Figure 18. Comparison of present experimental results with Al Arabi and Khamis data

6. Conclusions

In this detailed experimental investigation, an effect of thin cylinder inclination and diameter on natural convective heat transfer coefficient over the surface of electrically heated slender cylinders has been studied. Average value of Nusselt number was calculated for different configurations of thin cylinder. Study shows that heat transfer coefficient depends upon both the diameter and inclination of thin cylinders. Information in dimensionless form in this study may be useful for thermal design engineers in decision making processes. Main findings of the present study are given below:

1) Heat transfer coefficient increases significantly with decrease in diameter due to decrease in thermal boundaey layer.

2) Almost 30% increment in average Nusselt number was observed on vertical cylinder having 6.1 slenderness ratio as compared to the vertical flat plate.

3) Al-Arabi and Khamis correlation can be used with confidence for iso-flux heated cylinders having minimal end losses for $1.28 \times 10^8 \leq Ra^*_L \leq 1.08 \times 10^{10}$.

4) Heat transfer coefficient increases with increase in inclination angle - measured from vertical axis.

5) Experimental data is in good agreement with the already published data.

6) Axial smoke flow was observed in vertical configuration; cross smoke flow was observed in horizontal configuration while both type of flows were observed in inclined configuration of thin cylinder.

7) A slight external disturbance at the vicinity of thin cylinder may significantly increase the natural convection heat transfer. Therefore, it is advised to perform research study inside the enclosure.

Nomenclature

$A_{s\,(m^2)}$	Surface area	T_b (K)	Ambient or Bulk stream temperature
$C_{p\,(J.Kg.K^{-1})}$	Specific heat at constant pressure	$T_{f\,(K)}$	Film Temperature
$D\ (m)$	Outer surface diameter	$T_{s\,(K)}$	Surface temperature
Gr^*	Modified Grashof number	$V\ (v)$	Voltage
$g\ (m.s^{-2})$	Gravitational acceleration	$x\ (m)$	Distance from bottom of cylinder
$h\ (W.m^{-2}.K^{-1})$	Convective heat transfer coefficient	$\Theta\ (°)$	Angel of inclination of cylinder (from the vertical position)
$I\ (amp)$	Current	$B\ (K^{-1})$	Coefficient of volumetric expansion
$k\ (W.m^{-1}.K^{-1})$	Thermal conductivity	$P\ (Kg.m^{-3})$	Density
$L_{c\,(m)}$	Characteristic length	$A\ (m^2.s^{-1})$	Thermal diffusivity
Nu_L	Average Nusselt number	$\mu\ (kg.m^{-1}.s^{-1})$	Dynamic viscosity
Pr	Prandtl number	E	Emissivity
$Q\ (W)$	Thin cylinder power	$v\ (m^2.s^{-1})$	Kinematic viscosity
Ra^*	Modified Rayleigh number	$O\ (W.m^{-2}.K^{-4})$	Stefan Boltzmann constant
T_b (K)	Ambient or Bulk stream temperature	Λ	Dimensionless independent variable $[(y/R)^{0.8}/Gr_R]^{1/8}$

Conflict of Interest

There is no conflict of interest.

References

[1] Popopiel, C.O., 2008. Free Convection Heat Transfer from Vertical Slender Cylinders: A Review. Heat Transfer Engineering. 291(6), 521-536. DOI: https://doi.org/10.1080/01457630801891557

[2] Popiel, C., Wojtkowiak, J., Bober, K., 2007. Laminar Free Convective Heat Transfer from Isothermal Vertical Slender Cylinder. Experimental Thermal & Fluid Science. 32(2), 607-613. DOI: https://doi.org/10.1016/j.expthermflusci.2007.07.003

[3] Cebeci, T., 1974. Laminar Free Convection Heat Transfer from the Outer Surface of a Vertical Slender Circular Cylinder. Fifth Int Confer, Tokyo, Japan.

[4] Incropera, F.P., Dewitt, D.P., Bergman, T.L., et al., 2012. Fundamentals of Heat and Mass Transfer, John Wiley and Sons.

[5] Churchill, S., Chu, H., 1975. Correlating Equations for Laminar and Turbulent Free Convection from Vertical Flat Plate. International Journal of Heat and Mass Transfer. 18(11), 1323-1329.

[6] Oosthuizen, P.H., Paul, J.T., 2006. Natural Convective Heat Transfer from a Narrow Isothermal Vertical Flat Plate. Proceedings of the 9th AIAA/ASME Joint Thermophysics and Heat Transfer.

[7] Oosthuizen, P.H., Paul, J.T., 2007. Natural Convective Heat Transfer from a Narrow Vertical Flat Plate With a Uniform Heat Flux at the Surface. Proceedings of ASME-JSME Thermal Engineering Heat Transfer Summer Conference Collocated with the Asme Interpack Conference.

[8] Sparrow, E., Gregg, J., 1956. Laminar Free Convection Heat Transfer from the Outer Surface of a Vertical Circular Cylinder. ASME. 78, 1823-1829.

[9] Yang, S., 1985. General Correlating Equations for Free Convection Heat Transfer from a Vertical Cylinder. International Symposium on Heat Trans, Peking.

[10] Al-Arabi, M., Khamis, M., 1982. Natural Convection Heat Transfer from Inclined Cylinders. International Journal of Heat & Mass Transfer. 25(1), 3-15.

[11] Riaz, A., Shah, A., Bait, A., et al., 2019. Experimental Study of Laminar Natural Convection Heat Transfer from Slender Circular Cylinder in Air Quiescent Medium. International Bhurban Conference on Applied Sciences and Technology, Islamabad, Pakistan.

[12] Nusselt, W., 1929. Die Wärmeübgabe Eines Waagrecht Liegenden Drahtes Oder Rohres In Flüssigkeiten Und Gasen. Ver Deut Ing. 73, 1475-1478.

[13] Morgan, V.T., 1975. The Overall Convective Heat Transfer from Smooth Circular Cylinders. Advances in Heat Transfer. 11, 199-264.

[14] Dyer, J., 1965. Laminar Natural Convection from a Horizontal Cylinder with a Uniform Convective Heat Flux. Trans Inst Eng Aust. pp. 125-128.

[15] Oosthuizen, O., Mansingh, V., 1986. Free and Forced

Convection Heat Transfer from Short Inclined Circular Cylinders. Chemical Engineering Communications. 42(4-6), 333-348.

[16] Al-Arabi, M., Salman, Y., 1979. Laminar Natural Convection Heat Trnasfer from an Inclined Cylinders. International Journal of Heat & Mass Transfer. 23, 45-51.

[17] Cengel, Y.A., Ghaja, A.J., 2014. Heat and Mass Transfer, Fundamentals and Application, 5th ed., McGraw- Hill Education.

[18] Holman, J., 2002. Heat Transfer, vol. 9th, McGraw Hill.

[19] Chughtai, I., Natural Convection Heat Transfer Through Vertical Heated Cylinder Assemblies, Islamabad, Pakistan, 2016.

[20] Shaukatullah, H., Claassen, A., 2003. Effect of Thermocouple Wire Size and Attachement Method on Measurement of Thermal Characteristics of Electronic Packages. 19th IEEE SEMI-THERM Symposium.

[21] Lee, J.B., Kim, H.J., Kim, D.K., 2016. Experimental Study of Natural Convection Cooling of Vertical Cylinders with Inclined Plate Fins. Energies. 9(6), 391. DOI: https://doi.org/10.3390/en9060391

[22] Lee, H., Chen, T., Armaly, B., 1988. Natural Convection Along Slender Vertical Cylinder with Variable Surface Temperature. Journal of Heat Transfer. 110, 103-108.

[23] Jarall, S., Campo, A., 2007. Experimental Study of Natural Convection from Electrically Heated Vertical Cylinders Immersed in Air. Experimental Heat Transfer. 18(3).
DOI: https://doi.org/10.1080/08916150590953360

[24] Rohensow, W., Ganic, E., Cho, Y., 1998. Handbook of hea trasnfer, 3rd ed., New York: McGraw-Hill.

BILINGUAL PUBLISHING CO.
Pioneer of Global Academics Since 1984

Semiconductor Science and Information Devices
https://ojs.bilpublishing.com/index.php/ssid

ARTICLE

Electronic Structure of CdS Nanoparticles and CdSe/CdS Nanosystems

V. Zavodinsky[1*] O. Gorkusha[1] A. Kuz'menko[2]

1. Institute of Applied Mathematics, Khabarovsk Division, Khabarovsk, 680038, Russia
2. South-West State University, Kursk, 305040, Russia

ARTICLE INFO

Article history
Received: 10 May 2022
Revised: 07 July 2022
Accepted: 15 July 2022
Published Online: 12 August 2022

Keywords:
Nanoparticles
Cadmium sulfide
Cadmium selenide
Energy gap
Modeling with pseudopotentials

ABSTRACT

The electronic states of "wurtzite" CdS nanoparticles and CdSe/CdS nanosystems with up to 80 pairs of Cd-Se or CdS atoms were calculated. The results for CdS particles were compared with the results obtained earlier for CdSe particles of the same size and with published calculations of other authors. The calculated gap values in the range of 2.84 eV ~ 3.78 eV are typical for CdS particles of studied sizes in accordance with results of published data. The CdSe/CdS nanosystems were considered as layered ones and as quantum dots. The layered CdSe/CdS systems with two-layer CdS coverings can be interpreted in terms of combinations of two semiconductors with different energy band gaps (2.6 eV and 3.3 eV), while analogous systems with single-layer CdS coverings do not demonstrate a two-gap electron structure. Simulation of a CdSe/CdS quantum dot shows that the single-layer CdS shell demonstrates a tendency for the formation of the electronic structure with two energy gaps: approximately of 2.5 eV and 3.0 eV.

1. Introduction

Cadmium selenides and cadmium sulfides (CdSe and CdS), semiconductors with band gaps of about 1.8 eV and 2.4 eV, respectively are promising materials for optoelectronic devices [1-15]. X-ray diffraction analysis indicates that the structure of CdSe nanoparticles with sizes of 2.8 nm, 4.1 nm and 5.6 nm is wurtzite-like, and the energy gaps E_{gap} for these particles are 2.5 eV, 2.2 eV, and 2.0 eV, respectively [6]. Our calculations [16] confirm this conclusion. As for CdS nanoparticles they can have both sphalerite and wurtzite structures, depending on what sulphur source are used [8,10]. However, the wurtzite structure is energetically more favorable [17]. One main application of these substancies is their using in the core/shell CdSe/CdS quantum dots [18-22], in which an improved luminescence quantum yield is achieved, the fluorescence lifetime is reduced and the desired band gap is achieved, that is, a

*Corresponding Author:
V. Zavodinsky,
Institute of Applied Mathematics, Khabarovsk Division, Khabarovsk, 680038, Russia;
Email: vzavod@mail.ru

DOI: https://doi.org/10.30564/ssid.v4i2.4708

Copyright © 2022 by the author(s). Published by Bilingual Publishing Co. This is an open access article under the Creative Commons Attribution-NonCommercial 4.0 International (CC BY-NC 4.0) License. (https://creativecommons.org/licenses/by-nc/4.0/).

given wavelength of light radiation is provided.

Elecronic structure of CdS nanoparticles was studied in some works using the density functional theory (DFT) calculations. Mahesh M. Kamble et al. [8] obtained the energy gap of 2.38 eV ~ 2.65 eV for the wurtzite type particles; Soltani et al. [10] demostrated the gap close to 2.6 eV for the both wurtzite and sphalerite structure; Favero et al. [15] claimed that sphalrite nanoparticles were unstable but the wurtzite ones were stable with the energy gap of 1.8 eV.

The ab initio calculations for CdSe/CdS quantum dots were described in two works [21,22] the both works used a wurtzite structure. Romanova and Galyametdinov [21] studied the layered CdSe/CdS quantum dots in the frame of DFT; the CdSe/CdS monolayers ratio was taken as 3/7; the calculated two-band structure was found with gaps of 2.5 eV and 13 eV. Ying Luo and Lin-Wang Wang [22] investigated CdSe/CdS core/shell nanorods with 3063 atoms included the surface passivation pseudo-hydrogen atoms. They obtained the band gaps for CdS and CdSe are 2.079 eV and 1.414 eV, respectively.

In our recent work, we studied in detail the energy and electronic structure of CdSe nanoparticles [16] and found that, at small sizes (less than 2 nm), particles with a "rock-salt"-type structure are energetically favorable, however for larger nanoparticles, a "wurtzite"-type structure is preferable. The dependences of the energy gap width near the Fermi level on the particle size were also studied. In this work, we calculate the electronic structure of CdS nanoparticles in comparison with the results obtained for CdSe particles and study the electronic structure of CdSe/CdS layered nanosystems and quantum dots.

2. Modeling Technique

As in the previous work [16], the simulation was carried out using the FHI96md package [23] based on the DFT [24] and the pseudopotential approach; the calculation procedure was also similar. In particular, for Cd atoms, we used a 2-electron pseudopotential acting on two s-electrons, considering them to be valence, and referring ten d-electrons to be in the atomic core. It was shown [16] that this pseudopotential, in contrast to the 12-electron one, leads to correct values of the energy gap for nanoparticles. Pseudopotentials were generated using the FHI98pp package [25] with the local density approximation (LDA) [26,27] in the framework of the Troullier-Martins (TM) [28] scheme, as it was made studying the CdSe nanoparticles [16].

3. Results and Discussion

3.1 CdS Nanoparticles: Comparison with CdSe

Since the "wurtzite" phase (w-CdS) is the most stable one for cadmium sulfide [17], we studied CdS nanoparticles with this structure, taking them in the same form in which we took w-CdSe particles [16]. Atomic schemes of studied particles are shown in Figure 1.

Figure 1 shows that the atomic structure of w-CdS particles undergoes a significant change in the process of relaxation. The arrangement of cadmium atoms changes most significantly: the outer Cd atoms are shifted into the space between the S layers. The same conclusion was made by Favero et al. [15] who marked that the relaxated CdS nanoparticles are S-terminated. In addition, noticeable displacements of atoms in the lateral directions also occur.

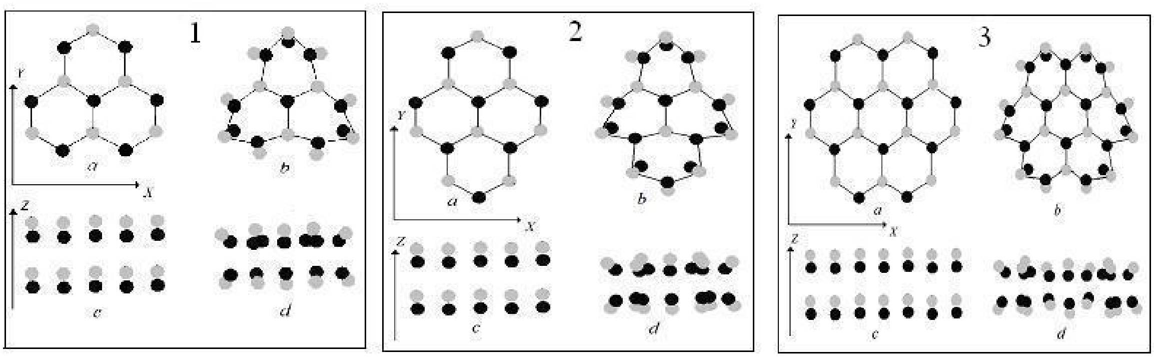

Figure 1. The structure schemes of the studied $(CdS)_n$ particles with the "wurtzite" structure

The numbers 1, 2, and 3 are the numbers of options. Schemes of particles of minimum sizes are shown: $(CdS)_{13}$ for option 1; $(CdS)_{16}$ for option 2); $(CdS)_{24}$ for option 3. The remaining particles are obtained by adding the appropriate number of layers along the Z axis. The letters indicate: a and b are views "from above" (in the XY plane); c and d are "side views" (along the Z axis). Option 1 corresponds to particles with n = 13, 26, 39, 52. Option 2 means particles with n = 16, 32, 48, 64, 80. Option 3 means particles with n = 24, 48, 72. Black spheres represent Cd atoms, gray spheres represent S atoms. In each panel, the left figures show the starting configurations, the right ones show the changed arrangement of atoms as a result of relaxation.

Calculations showed that, in accordance with the experimental data [12-14], the energy gap E_{gap} for w-CdS particles decreases with increasing particle size, similarly to how it occurs in the case of w-CdSe particles [16]. Table 1 demonstrates our calculation results in comparing with previous results for w-CdSe particles [16].

It can be seen from this Table that, in general, in each option, the gap width decreases with increasing particle size, however, an increase in the size in the lateral direction can lead to an increase in the gap width with the same number of atoms (the case: n = 48, options 2 and 3). In all cases, as expected, the gap is wider for cadmium sulfide particles than for cadmium selenide ones of the same size and shape. We also note that our values of the gap (from 2.84 eV up to 3.78 eV) are typical for CdS particles of such sizes [6,13], therefore, we can trust our calculation methodology.

3.2 Electronic Structure of CdSe/CdS Layered Nanosystems

To study the electronic structure of the layered CdSe/CdS nanosystems, we took CdSe particles from all three options presented in Figure 1 as a basis and added CdS layers to them as covering. The constructed particles are as follows: A) two $Cd_{13}Se_{13}$ layers between two single layers $Cd_{13}S_{13}$ (option 1, N=104); B) four Cd_8Se_8 layers between two single Cd_8S_8 layers (option 2, N=96); C) four Cd_8Se_8 layers between two double $Cd_{16}S_{16}$ layers (option 2, N=128); D) two $Cd_{12}Se_{12}$ layers between two double $Cd_{24}S_{24}$ layers (option 3, N=144). The calculated values of the energy gap are collected in Table 2.

From this Table, we see that for the same number of atoms N, the value of E_{gap} increases when CdSe surface layers are replaced by CdS layers. However, since these systems are compounds of two materials with different band gaps, the question arises: Is a certain common electronic structure established in the entire CdSe/CdS nanosystem or is it formed differently in layers of different compositions?

To answer this question, we studied the local (layer-by-layer) electronic structure, using as examples the cases of a single-layer coating (B) and a doble-layer coating (C) and plotted the local densities of electronic states (LDOS) in Figure 2 in comparison with the total densities of electronic states (DOS).

An analysis of Figure 2 (B panels) shows that, when applying a single-layer coating, a different energy gap is not formed in the CdS layer, it is the same as in the CdSe layers (2.6 eV). We see that all LDOS's near the gap are very similar to each other and to those of the total DOS. On the other hand, panels C show that, in the case of the two-layer coating, a special energy gap of 3.3 eV is formed in the CdS layers (panels C2 and C3), and it is wider than the gap of 2.6 eV in the CdSe layers (panels C4 and C5) and in the total DOS spectrum (panel C1). One can see that the spectra in panels C2 and C3 lack the peaks of occupied states, which are marked by arrows in panels C1, C4, and C5. In other words, we see that this system is actually a combination of two semiconductors with two different band gaps.

3.3 Simulation of a CdSe/CdS Quantum Dot

To model a CdSe/CdS quantum dot we took the $Cd_{72}Se_{72}$ particle (option 3) and replaced surface Se atoms with S atoms. As a first step we constructed the $Cd_{48}Se_{48}+2\cdot Cd_{12}S_{12}$ system where only the topest and lowest Se atoms were replaced with S ones. Secondly, we made the $Cd_{24}Se_{24}+Cd_{48}S_{48}$ system, in which the $Cd_{24}Se_{24}$ core was completely capped by the $Cd_{48}S_{48}$ single-layer shell from all sides. We calculated the local densities of states and plotted results in Figure 3.

Table 1. Energy gap widths (in eV) for $(CdSe)_n$ and $(CdS)_n$ particles with the "wurtzite" structure for different particle shapes (options).

	Option 1				Option 2				Option 3		
n	13	26	39	52	16	32	48	64	24	48	72
$(CdSe)_n$	3.26	2.96	2.55	1.87	3.25	2.72	2.35	2.15	3.00	2.96	2.36
$(CdS)_n$	3.57	3.32	3.16	2.84	3.78	3.54	3.25	3.01	3.74	3.54	3.39

Table 2. The energy gap widths (in eV) calculated for CdSe/CdS layered nanosystems. For comparison, the results for the Cd_nSe_n particles of the same size (with the same total number of atoms: 2n=N) are given.

N=104		N=96		N=128		N=144	
A	$Cd_{52}Se_{52}$	B	$Cd_{48}Se_{48}$	C	$Cd_{64}Se_{64}$	D	$Cd_{72}Se_{72}$
2.18	1.87	2.75	2.48	2.80	2.15	2.62	2.36

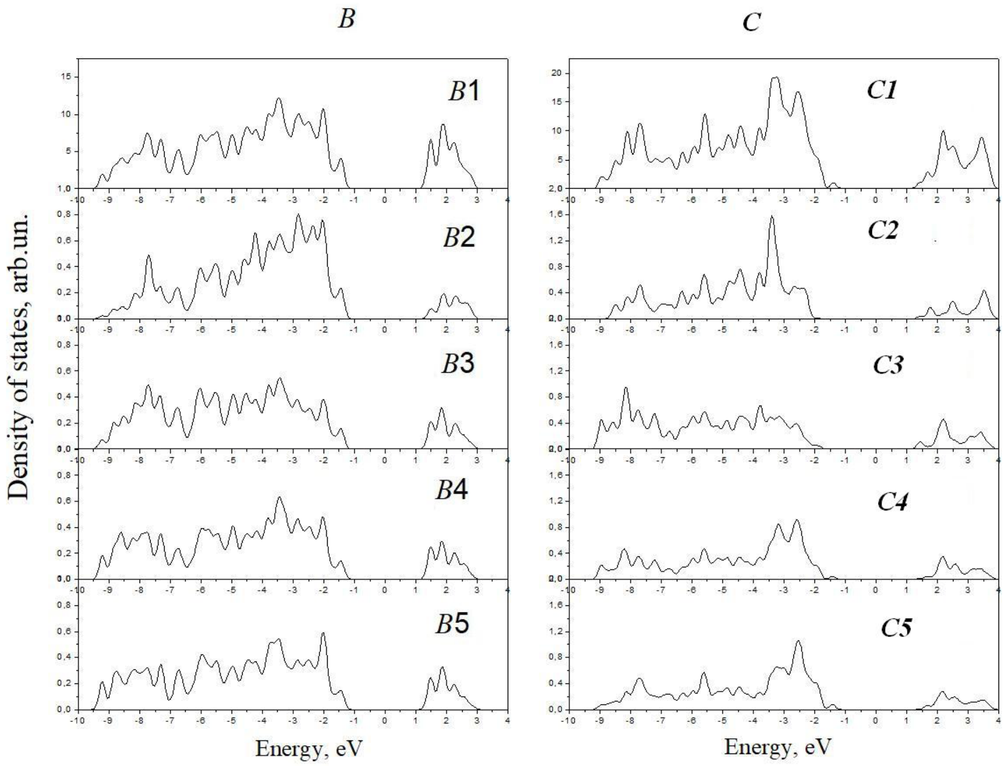

Figure 2. Densities of states (DOS) and local densities of states (LDOS) for studied nanosystems.

B: a single-layer coating. B1: the total DOS for the single-layer coating; B2: LDOS for the CdS layer of the a single-layer coating; B3: LDOS for the first CdSe layer in the single-layer coating system; B4: LDOS for the second CdSe layer in the single-layer coating system; B5: LDOS for the third CdSe layer in the single-layer coating system. C: a two-layer coating. C1: the total DOS for the two-layer coating; C2: LDOS for the first CdS layer of the two-layer coating; C3: LDOS for the second CdS layer of the two-layer coating; C4: LDOS for the first CdSe layer in the two-layer coating system; C5: LDOS for the third CdSe layer in the two-layer coating system.

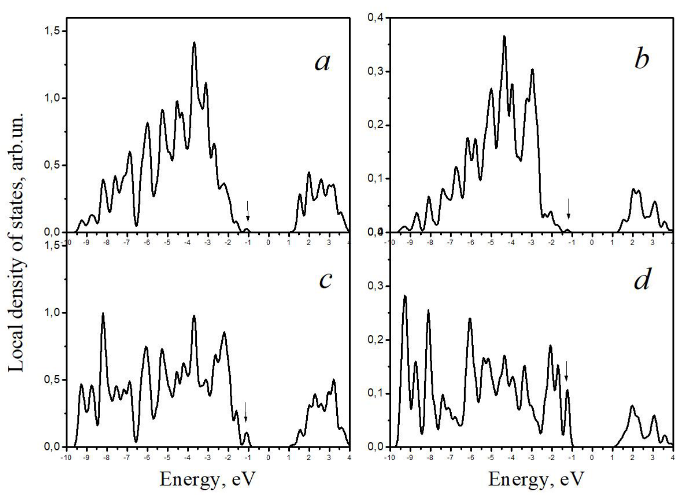

Figure 3. Local densities of states for the CdSe/CdS systems

a) the LDOS for the surface CdS layer of the $Cd_{48}Se_{48}+2\cdot Cd_{12}S_{12}$ layered system; b) the LDOS for the CdS shell atoms of the $Cd_{24}Se_{24}+Cd_{48}S_{48}$ quantum dot; c) the LDOS for the middle CdSe layer of the $Cd_{48}Se_{48}+2\cdot Cd_{12}S_{12}$ layered system; d) the LDOS for the CdSe core atoms of the $Cd_{24}Se_{24}+Cd_{48}S_{48}$ quantum dot. Arrows mark peaks of the highest occupied states.

We see in Figure 3 that a peak of the highest occupied states in the LDOS of the CdS cover layer (panel a) has a rather less intensity than an analogous peak in the LDOS of the middle CdSe layer (panel c). This means that in this system there is a tendency to form a wider energy gap. This trend is even more clearly seen in Figure 3 (panels b and d), where results for the $Cd_{24}Se_{24}$+$Cd_{48}S_{48}$ quantum dot with E_{gap} of 2.5 eV are presented. We see that the LDOS of the CdSe core (panel d) has a very intensive peak of the highest occupied states. These results together with ones described in the previous subsection allow us to think that if the CdS shell thickness increases to two layers, a different band gap will be formed in it, and this gap will be wider than that in the CdSe core (approximately up to 3 eV).

4. Conclusions

Our density functional pseudopotential study shows that the energy gap width E_{gap} of w-CdS nanoparticles decreases with increasing particle size in agreement with experiments. The calculated width values in the range of 2.84 eV ~ 3.78 eV are typical for particles of studied sizes in accordance with results of published data. In the CdSe/CdS nanosystems E_{gap} increases when the number of sulfur atoms increases. The electronic structures of the layered CdSe/CdS nanosystems with a single-layer CdS covering demonstrate a tendency to form the electron structure with two different energy gaps. The CdSe/CdS systems with two-layer CdS covering can be interpreted in terms of combinations of two semiconductors with different energy band gaps. Simulation of a quantum dot with a single-layer shell showed that the tendency to form two energy gaps in its electronic structure is much more pronounced than in a layered system with a single-layer double-sided coating.

On the whole, as a benefit of this study, our calculations predict that two-layer CdS shells are sufficient for the formation of the electronic structure with two energy gaps in the CdSe/CdS quantum dots. The results obtained can be useful in designing optical systems based on CdSe.

Conflict of Interest

There is no conflict of interest.

References

[1] Rani, S., Thanka Rajan, S., Shanthi, J., et al., 2015. Review on the materials properties and photoelctrochemical (PEC) solar cells of CdSe, $Cd_{1-x}Zn_xSe$, $Cd_{1-x}In_xSe$, thin films. Materials Science Forum. 832, 1-27.
DOI: https://doi.org/10.4028/www.scientific.net/MSF.832.1

[2] Rosmani, C.H., Zainurul, A.Z., Rusop, M., et al., 2014. The Optical and Electrical Properties of CdSe Nanoparticles. Advanced Materials Research. 832, 557-561.
DOI: https://doi.org/10.4028/www.scientific.net/AMR.832.557

[3] Abbassi, A., Zarhri, Z., Azahaf, Ch., et al., 2015. Boltzmann equations and ab initio calculations: comparative study of cubic and wurtzite CdSe. SpringerPlus. 4, 543.
DOI: https://doi.org/10.1186/s40064-015-1321-z

[4] Hu, J.T., Wang, L.W., Li, L.Sh., et al., 2002. Semiempirical Pseudopotential Calculation of Electronic States of CdSe Quantum Rods. The Journal of Physical Chemistry B. 106, 2447-2452.
DOI: https://doi.org/10.1021/jp013204q

[5] Proshchenko, V., Dahnovsky, Y., 2014. Spectroscopic and electronic structure properties of CdSe nanocrystals: spheres and cubes. Physical Chemistry Chemical Physics. 16, 7555-7561.
DOI: https://doi.org/10.1039/C3CP55314K

[6] S. Neeleshwar, C.L., Chen, C.B., Tsai, Y.Y., et al., 2005. Size-dependent properties of CdSe quantum dots. Physical Review B. 71, 201307(1-4).
DOI: https://doi.org/10.1103/PhysRevB.71.201307

[7] Ali, S.K., Wani, H., Upadhyay C., et al., 2020. Synthesis of CdS Nanoparticles by Chemical Co-precipitation Method and its Comparative Analysis of Particle Size via Structural and OpticalCharacterization. Indonesian Physical Review. 3(3), 100-110.
DOI: https://doi.org/10.29303/ipr.v3i3.64

[8] Kamble, M.M., Rondiya, S.R., Bade, B.R., et al., 2020. Optical, structural and morphological study of CdS nanoparticles: role of sulfur source. Nanomaterials and Energy. 9(1), 72-81.
DOI: https://doi.org/10.1680/jnaen.19.00041

[9] Edossa, T.G., Woldemariam, M.M., 2020. Electronic, structural, and optical properties of zinc blende and wurtzite cadmium sulfide (CdS) using density functional theory. Advances in Condensed Matter Physics. 2020.
DOI: https://doi.org/10.1155/2020/4693654

[10] Soltani, N., Gharibshahi, E., Saion, E., 2012. Band gap of cubic and hexagonal CdS quantum dots. Experimental and theoretical studies. Chalcogenide Letters. 9(7), 321-328.

[11] Khan, Z.R., Zulfequar, M., Khan, M.S., 2011. Chemical synthesis of CdS nanoparticles and their optical and dielectric studies. Journal of Materials Science.

46, 5412-5416.
DOI: https://doi.org/10.1007/s10853-011-5481-0

[12] Qi, L.M., Cölfen, H., Antonietti, M., 2001. Synthesis and characterization of CdS nanoparticles stabilized by double-hydrophilic block copolymers. Nano Letters. 1(2), 61-65.
DOI: https://doi.org/10.1021/nl0055052

[13] Muradov, M., Goncha, E., Bagirov, A., 2007. The effect of solutions concentrations on the optical properties of CdS nanoparticles formed in the polymeric matrix. Journal of Optoelectronics and Advanced Materials. 9(5), 1411-1413.

[14] Thakur, S., Kaur, R., Mandal, S.K., 2021. Size dependence of CdS nanoparticles on the precursor concentration and visible light driven photocatalytic degradation of methylene blue. New Journal of Chemistry. 45(27), 12227-12235.
DOI: https://doi.org/10.1039/d1nj01588e

[15] Favero, P.P., de Souza-Parise, M., Fernandez, J.L.R., et al., 2006. Surface Properties of CdS Nanoparticles. Brazilian Journal of Physics. 36(3B), 1032-1034.
DOI: https://doi.org/10.1590/S0103-97332006000600062

[16] Zavodinsky, V., Gorkusha, O., Kuz'menko, A., 2022. Total energy and electronic states of CdSe nanoparticles. Semiconductor Science and Information Devices. 4(1).
DOI: https://doi.org/10.30564/ssid.v4i1.4420

[17] Berger, L.I., 1997. Semiconductor Materials, CRC Press, New York, NY, USA, 1st edition.

[18] Zhou, W.L., Cai, T., Chen, Y., et al., 2014. Synthesis of CdS-Capped CdSe Nanocrystals without any Poisonous Materials. Advanced Materials Research. 981, 806-809.
DOI: https://doi.org/10.4028/www.scientific.net/AMR.981.806

[19] Sarkar, P., Springborg, M., Seifert, G., 2005. A theoretical study of the structural and electronic properties of CdSe/CdS and CdS/CdSe core/shell nanoparticles. Chemical Physics Letters. 405, 103-107.
DOI: https://doi.org/10.1016/j.cplett.2005.02.001

[20] Dmitri, V., Talapin, J.H., Nelson, E.V., et al., 2007. Seeded growth of highly luminescent CdSe/CdS nanoheterostructures with rod and tetrapod morphologies. Nanoletters. 7(10), 2951-2959.
DOI: https://doi.org/10.1021/nl072003g

[21] Romanova, K.A., Galyametdinov, Y.G., 2021. Quantum-chemical study of CdSe/CdS core/shell and CdSe/CdS/ZnS core/shell/shell quantum dots with different layers ratio. AIP Conference Proceedings 2380, 060001.
DOI: https://doi.org/10.1063/5.0058295

[22] Luo, Y., Wang, L.W., 2010. Electronic Structures of the CdSe/CdS Core-Shell Nanorods. ACS Nano. 4(1), 91-98.
DOI: https://doi.org/10.1021/nn9010279

[23] Beckstedte, M., Kley, A., Neugebauer, J., et al., 1997. Density functional theory calculations for poly-atomic systems: electronic structure, static and elastic properties and ab initio molecular dynamic. Computer Physics Communications. 107, 187-205.
DOI: https://doi.org/10.1016/S0010-4655(97)00117-3

[24] Kohn, W., Sham, J.L., 1965. Self-consistent equations including exchange and correlation effects. Physical Review. 140, A1133-A1138.
DOI: https://doi.org/10.1103/PhysRev.140.A1133

[25] Fuchs, M., Scheffler, M., 1999. Ab initio pseudopotentials for electronic structure calculations of poly-atomic systems using density functional theory. Computer Physics Communications. 119, 67-165.
DOI: https://doi.org/10.1016/S0010-4655(98)00201-X

[26] Perdew, J.P., Wang, Y., 1986. Accurate and simple density functional for the electronic exchange energy. Physical Review B. 33, 8800-8802.
DOI: https://doi.org/10.1103/PhysRevB.33.8800

[27] Ceperly, D.M., Alder, B.J., 1980. Ground state of the electron gas by a stochastic method. Physical Review Letters. 45, 566-569.
DOI: https://doi.org/10.1103/PhysRevLett.45.566

[28] Troullier, N., Martins, J.I., 1991. Efficient pseudopotentials for plane-wave calculations. Physical Review B. 43, 1993-2006.
DOI: https://doi.org/10.1103/PhysRevB.43.1993

BILINGUAL PUBLISHING CO.
Pioneer of Global Academics Since 1984

Semiconductor Science and Information Devices
https://ojs.bilpublishing.com/index.php/ssid

ARTICLE

Air Pollution Monitoring System Using Micro Controller Atmega 32A and MQ135 Gas Sensor at Chandragiri Municipality of Kathmandu City

Rajesh Shrestha* **Manik Maharjan** **Mahesh Sharma**

Tri-Chandra Multiple Campus, Kathmandu, Nepal

ARTICLE INFO

Article history
Received: 12 July 2022
Revised: 3 September 2022
Accepted: 13 September 2022
Published Online: 9 October 2022

Keywords:
Arduino Uno
MQ135 sensor
Air pollution
I2C display
Atmosphere

ABSTRACT

Air is one of the essential elements of human's surroundings. The earth's atmosphere is full of air which contains gases such as Nitrogen, Oxygen, Carbon Monoxide and traces of some rare elements. But quality of the air has been degrading for some decades due to various activities conducted by the human beings that directly or indirectly affect the atmosphere leading to the air pollution. There are different techniques to measure air quality. However, with the evolution of time the expensive and less efficient analog devices have been replaced by more efficient and less expensive electronics device. In this research, MQ135 sensor is used to measure air quality of a particular location. I2C display is used to monitor the data. Indeed, with the increasing in number of vehicles, unplanned urbanization and rapid population growth, air pollution has considerably increased in the last decades in various areas of Kathmandu. Thus, this project 'Air Pollution Monitoring System' was focused on collection of the data specific location of Chandragiri municipality of Kathmandu city. In conclusion, analysis of the data is done with the help of origin software which shows that the Arduino device in this device works perfectly for measuring the air pollution. Air quality of the selected area is found to be less than 500 PPM which concludes that the air quality of this area is normal.

1. Introduction

Air is one of the essential elements of human's surroundings. The earth's atmosphere is full of air which contains gases such as Nitrogen, Oxygen, Carbon Monoxide and traces of some rare elements. Humans, animals as well as plants need an atmosphere of air that is free from contaminants which is very crucial for human life and health. But quality of the air has been degrading for some decades due to various activities conducted by the human beings that directly or indirectly affect the atmosphere leading to the air pollution. Air pollution is the biggest problem of every nation, whether it is developed or developing. IoT based air pollution monitoring system was developed and used to monitor and collect the data related to air pollution. Wi-Fi module ESP8266 was used to con-

*Corresponding Author:
Rajesh Shrestha,
Tri-Chandra Multiple Campus, Kathmandu, Nepal;
Email: rajeshshrestha402@gmail.com

DOI: https://doi.org/10.30564/ssid.v4i2.4884
Copyright © 2022 by the author(s). Published by Bilingual Publishing Co. This is an open access article under the Creative Commons Attribution-NonCommercial 4.0 International (CC BY-NC 4.0) License. (https://creativecommons.org/licenses/by-nc/4.0/).

nect the system with the internet. It showed the air quality in PPM on the LCD. It can be used easily to check the air quality of the specific areas in real time [1].

According to World Health Organization (WHO), air pollution is defined as contamination of the indoor or outdoor environment by any chemical, physical, or biological agent that modifies the natural characteristics of the atmosphere. Common sources of air pollution are household combustion devices, motor vehicles, industrial facilities, unplanned urbanization, rapid population growth and forest fires [2]. Air pollution is the presence of extra unwanted biological molecules, particulates or other harmful things into the earth atmosphere. It is a major cause of infections, allergies, and eventually reasons of death to some peoples. A variety of respiratory and other diseases, which can also be fatal, are caused by outdoor and indoor air pollution. The world health organization (WHO) in 2014 approximated those 7 million people deaths worldwide because of air pollution [3].

Air pollution is a complex mixture of thousands of components, majority of which include airborne Particulate Matter (PM) and gaseous pollutants like ozone (O_3), nitrogen dioxide (NO_2), volatile organic compounds (like benzene), carbon monoxide (CO), sulfur dioxide (SO_2), etc. [4].

Day by day the air is degrading in a dangerous manner. Same rate of degradation may lead to not only environment degradation but also affect the health of the human beings and other living organisms. So, minimization and control of air pollution and alerting people about the growing air pollution is of significant importance to alleviate particular actions to limit it [5].

Sensors have become less expensive, smaller, and more energy efficient as sensing, processing, and transmission technologies have advanced. However, WSN system performance is still influenced by unit computation speed, memory capacity, and connection stability, among other factors. Many difficulties in WSN software, such as routing protocols, media access control, coverage, and power management, have been discussed in conjunction with hardware restrictions [6]. A sensor node is made up of several parts, such as a transmitter, data processing components, receivers, and an energy supply. Sensor nodes are in charge of sending information discovered through their sensing abilities to following sensor nodes or sink nodes. The sensor component of the system measures a variety of environmental characteristics such as gases, smoke concentrations, and dust particles, among others [7].

2. Literature Review

Innumerable works had been carried out till today throughout the world regarding air pollution monitoring system. Air pollution and air quality in real time has been monitored with different process and methodology be using different devices and software [8]. To measure the air quality, similar work has been done with IoT based system by using data processing node (Raspberry's Pi). MQ135 sensor has been used to measure air quality. The data are stored in Raspberry's Pi and displayed on-screen and on other devices. The python code has been used to operate with Raspberry Pi. However, Raspberry pi is very expensive as compared to the Arduino board. Arduino is cheap and easy to use for students or researchers [9].

Similarly, air pollution monitoring system based on IoT and artificial intelligence has been developed which gather the data and alert the personnel immediately while the threshold level of pollution exceeds. This system fulfilled the humanitarian need by tracking the quality of air that people breadth in high traffic areas and possessed a health risk by alerting people to unhealthy level of these sensed pollutants. It is a low-cost and high-fidelity air quality monitoring system that can be used in school areas, in factories as well as in hospital areas [10].

Likewise, another device Arduino-based real time air quality and pollution detector has been developed. It has used MQ135 as a gas sensor which is linked with Arduino Uno board. This system has checked the air quality of cigarette smoke, coil burning smoke, vehicle smoke from street etc. with respect to time and the distance. This system can be developed and used even by students since it is reliable as well as low costing for collecting and analyzing the data related to air pollution [11].

Further, IoT based air pollution monitoring system had been developed. This system used on Arduino Uno R13 microcontroller as air pollution monitoring equipment. Arduino Uno device is connected with ESP8266 module which is an extremely cost-effective board. This IoT based project allows us to monitor the pollution level of anywhere by using computer or mobile phone [12].

Another research '*Smart Environment Monitoring System by employing Wireless Sensor Networks on Vehicles for Pollution Free Smart Cities*' has been carried out. This research introduced the concept with inclusion of the Internet of Things and LTE-M modules that are low cost and more efficient system. It is more effective but expensive comparing to air monitoring device based on Arduino Uno [13].

In similar way, low power wide area (LPWA) technology, an emerging Machine-to-Machine (M2M) communications technique was used to develop the air pollution monitoring system. With the aid of the LPWA network, the air sensing data over a large coverage area is collected and transmitted to the IoT cloud in time [14].

3. Materials and Methods

3.1 Working Method of Air Pollution Monitoring System

In this system, MQ135 sensor is used to sense the air quality. The data collected by the sensor are received by Arduino Uno. Then the data so collected are displayed on I2C LCD display. Similarly, EPS8266 module connects Arduino to internet so that the data are regularly updated on the internet as well. LED lights also used to notify the level of air quality based on PPM of air pollution.

Figure 1 given below shows the block diagram of Air Pollution Monitoring System. It shows how the device works using Arduino Uno with air sensor MQ135.

Figure 1. Block Diagram of Air Pollution Monitoring System

3.2 Circuit Diagram and Working Explanation

The circuit diagram of Air Pollution Monitoring System using Arduino Uno is as shown in the figure. MQ135 sensor is connected to Arduino to measure the value of air quality of the surrounding. In this circuit, SCL and SDA are connected to analog input A4 and A5 port of Arduino respectively. Negative terminal of MQ 135 sensor is grounded and positive terminal is connected to A3 port of Arduino. The orange wire of the sensor is connected to the VCC of I2C and gray wire of I2C is grounded. Positive terminal of red, green and yellow LEDs are connected to 3, 4 and 5 port of digital (pwm) and negative terminal of terminal of red, green and yellow LED are grounded in Bread GND pin. Breadboard is powered from Arduino power pin.7 – 12 v DC power is supplied to Arduino with the help of power bank. The data collected by the sensors are directed toward I2C through Arduino and displayed in the I2C.

Given Figure 2 represents the circuit diagram of air pollution monitoring system, the figure is designed using fritzing software. It shows the connection of Arduino Uno corresponding to I2C display, LED lights and MQ135 sensors.

3.3 Field Observation and Data Collection

After constructing the device, field observation was done to test the device. Related data were collected form Chandragiri-10, Boshigaun which lies on the southern part of the Kathmandu city. Data of three different loca-

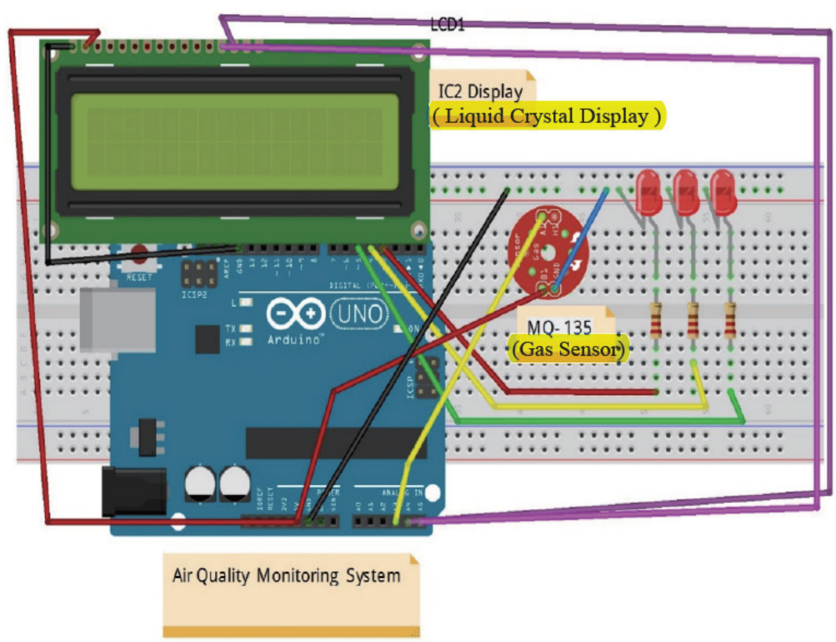

Figure 2. Circuit Diagram of Air Pollution Monitoring System

tions, Basic Learning English Secondary School, Buddha Chowk periphery and Khushi Khushi chowk within Chandragiri-10, Boshigaun were collected to observe the air quality of Chandragiri-10, Boshigaun. Data were collected for 30 minutes for three different time in morning, day and evening. Data during morning, day and evening were collected at exactly same time in three different locations.

On 2022/03/25, data were collected for 30 minutes during morning, day and evening time at 7:00 AM – 7:30 AM, 1:00 PM – 1:30 PM and 6:00 PM – 6:30 PM form Basic Learning English Secondary School.

Data collected at Basic Learning English Secondary School are shown in Table 1 below:

Table 1. Data collected at Basic Learning English Secondary School using Air Pollution Monitoring System

Morning		Day		Evening	
Time	PPM	Time	PPM	Time	PPM
7:00 AM	395	1:00 PM	342	6:00 PM	225
7:01 AM	381	1:01 PM	335	6:01 PM	230
7:02 AM	375	1:02 PM	331	6:02 PM	221
7:03 AM	363	1:03 PM	335	6:03 PM	223
7:05 AM	355	1:05 PM	312	6:05 PM	219
7:06 AM	353	1:06 PM	309	6:06 PM	217
7:07 AM	333	1:07 PM	304	6:07 PM	213
7:09 AM	315	1:09 PM	299	6:09 PM	218
7:10 AM	309	1:10 PM	295	6:10 PM	210
7:11 AM	305	1:11 PM	290	6:11 PM	209
7:12 AM	304	1:12 PM	291	6:12 PM	211
7:14 AM	302	1:14 PM	292	6:14 PM	216
7:15 AM	303	1:15 PM	294	6:15 PM	218
7:16 AM	307	1:16 PM	265	6:16 PM	219
7:18 AM	314	1:18 PM	301	6:18 PM	209
7:19 AM	323	1:19 PM	299	6:19 PM	206
7:20 AM	327	1:20 PM	300	6:20 PM	203
7:21 AM	328	1:21 PM	296	6:21 PM	205
7:23 AM	325	1:23 PM	288	6:23 PM	199
7:24 AM	330	1:24 PM	290	6:24 PM	206
7:25 AM	341	1:25 PM	292	6:25 PM	203
7:26 AM	343	1:26 PM	293	6:26 PM	199
7:28 AM	320	1:28 PM	299	6:28 PM	200
7:29 AM	315	1:29 PM	302	6:29 PM	197

Data collected at Buddha Chowk periphery are shown in below Table 2:

Table 2. Data collected at Buddha chowk Periphery using Air Pollution Monitoring System

Morning		Day		Evening	
Time	PPM	Time	PPM	Time	PPM
7:00 AM	507	1:00 PM	408	6:00 PM	238
7:01 AM	497	1:01 PM	387	6:01 PM	231
7:02 AM	492	1:02 PM	366	6:02 PM	229
7:03 AM	445	1:03 PM	347	6:03 PM	225
7:05 AM	400	1:05 PM	320	6:05 PM	217
7:06 AM	387	1:06 PM	311	6:06 PM	209
7:07 AM	394	1:07 PM	293	6:07 PM	211
7:09 AM	343	1:09 PM	277	6:09 PM	208
7:10 AM	330	1:10 PM	293	6:10 PM	205
7:11 AM	312	1:11 PM	293	6:11 PM	204
7:12 AM	300	1:12 PM	285	6:12 PM	202
7:14 AM	296	1:14 PM	284	6:14 PM	201
7:15 AM	281	1:15 PM	289	6:15 PM	198
7:16 AM	275	1:16 PM	293	6:16 PM	198
7:17 AM	276	1:17 PM	281	6:17 PM	200
7:19 AM	258	1:19 PM	283	6:19 PM	200
7:20 AM	249	1:20 PM	279	6:20 PM	199
7:21 AM	255	1:21 PM	277	6:21 PM	201
7:22 AM	251	1:22 PM	274	6:22 PM	203
7:24 AM	250	1:24 PM	263	6:24 PM	200
7:25 AM	244	1:25 PM	260	6:25 PM	199
7:26 AM	239	1:26 PM	257	6:26 PM	198
7:28 AM	232	1:28 PM	254	6:28 PM	201
7:29 AM	227	1:29 PM	252	6:29 PM	200

Data collected at Khushi Khushi chowk are shown in Table 3 below:

Table 3. Data collected at Khushi Khushi Chowk using Air Pollution Monitoring System

Morning		Day		Evening	
Time	PPM	Time	PPM	Time	PPM
7:00 AM	520	1:00 PM	443	6:00 PM	251
7:01 AM	509	1:01 PM	420	6:01 PM	289
7:02 AM	499	1:02 PM	415	6:02 PM	287
7:03 AM	498	1:03 PM	425	6:03 PM	288
7:05 AM	488	1:05 PM	397	6:05 PM	274
7:06 AM	481	1:06 PM	405	6:06 PM	270
7:07 AM	475	1:07 PM	406	6:07 PM	268

Table 3 continued

Morning		Day		Evening	
Time	PPM	Time	PPM	Time	PPM
7:09 AM	476	1:09 PM	380	6:09 PM	267
7:10 AM	468	1:10 PM	379	6:10 PM	265
7:11 AM	459	1:11 PM	381	6:11 PM	258
7:13 AM	448	1:13 PM	371	6:13 PM	254
7:14 AM	440	1:14 PM	368	6:14 PM	253
7:15 AM	438	1:15 PM	345	6:15 PM	252
7:16 AM	431	1:16 PM	349	6:16 PM	253
7:17 AM	425	1:17 PM	339	6:17 PM	251
7:19 AM	412	1:19 PM	305	6:19 PM	249
7:20 AM	408	1:20 PM	295	6:20 PM	248
7:21 AM	399	1:21 PM	285	6:21 PM	246
7:23 AM	376	1:23 PM	275	6:23 PM	246
7:24 AM	379	1:24 PM	289	6:24 PM	248
7:25 AM	370	1:25 PM	290	6:25 PM	249
7:26 AM	375	1:26 PM	281	6:26 PM	247
7:27 AM	366	1:27 PM	279	6:27 PM	246
7:28 AM	358	1:28 PM	275	6:28 PM	245
7:29 AM	350	1:29 PM	282	6:29 PM	244

4. Result and Discussion

This Air Pollution Monitoring System has been constructed by connecting sensor and other different components to Arduino Uno in a breadboard with the help of jumper wires.

Figure 3 shows the construction of the air pollution monitoring device. It also shows the connection of the Arduino Uno with I2C display.

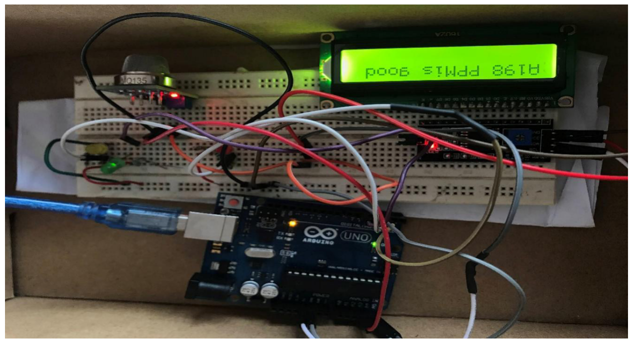

Figure 3. Arduino Uno connected with I2C display

Following variation of air quality in PPM were obtained with respect to time.

4.1 Result Obtained from Basic Learning English Secondary School Periphery Using Arduino Based Device

Figure 4 below represents the variation of PPM with respect to particular time of the data collected from the Basic Learning English Secondary School. This figure shows that the air quality of this location is better as PPM is below 500.

4.2 Result Obtained from Buddha Chowk Periphery Using Arduino Based Device

Figure 5 represents the variation of air quality obtained during those phases of time with the help of data collected from Buddha Chowk periphery. This figure shows that the maximum PPM of this location during a day is 500. In this location data were recorded on 2022/04/03 during morning, day and evening time within 7 AM to 6:30 PM.

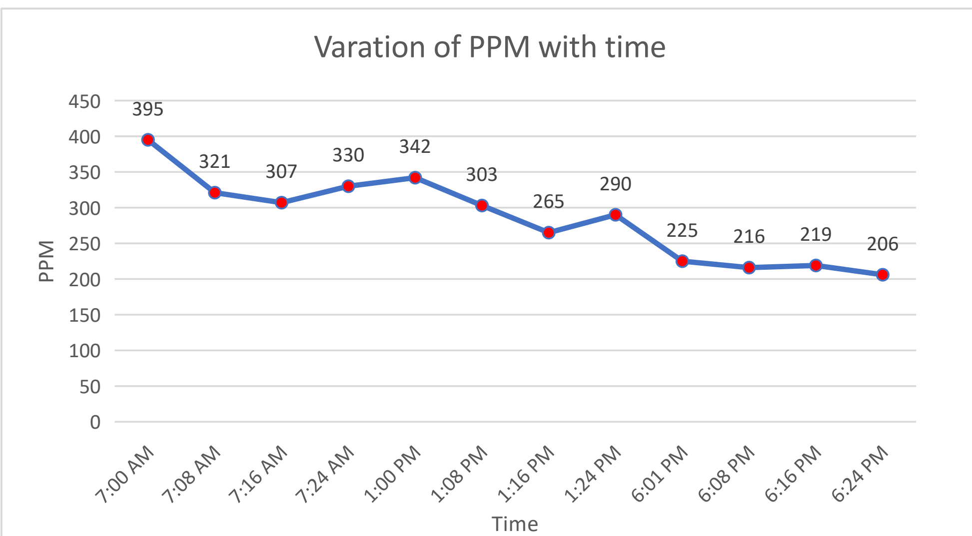

Figure 4. Variation of PPM with respect to time obtained from data recorded at Basic Learning Secondary School

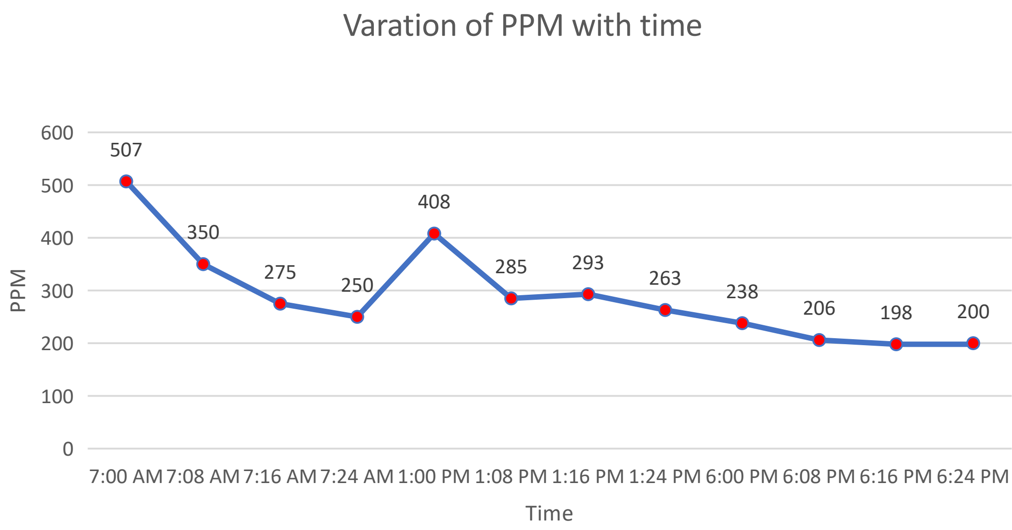

Figure 5. Variation of PPM with respect to time obtained from data recorded at Buddha Chowk Periphery

4.3 Result Obtained from Khushi Khushi Chowk Using Arduino Based Device

Figure 6 shows the variation of PPM with respect to time of Khushi Khushi Chowk. In this location data were recorded on 2022/04/03 during morning, day and evening time.

4.4 Comparison of PPM Obtained from Three Different Locations of Boshigaun

After collection of data from three different locations at exactly same time, obtained data were compared and shown in below graph.

Figure 7 represent the graph which shows the comparison of the PPM of three different location from where the data are collected. It shows that the PPM is high during morning time and gradually decreases till the evening of all three locations.

4.5 Analysis of Data

The data obtained using Arduino have been analyzed and calculation of error has been done with the help of origin software.

The analysis of the data recorded at school periphery using origin software is shown in the graph below:

Figure 8 represents the graph of linear fitting and polynomial fitting fitted between air quality (PPM) and time of Basic Learning English Secondary School.

Table 4 shows the standard error of linear fitting of the data obtained from school.

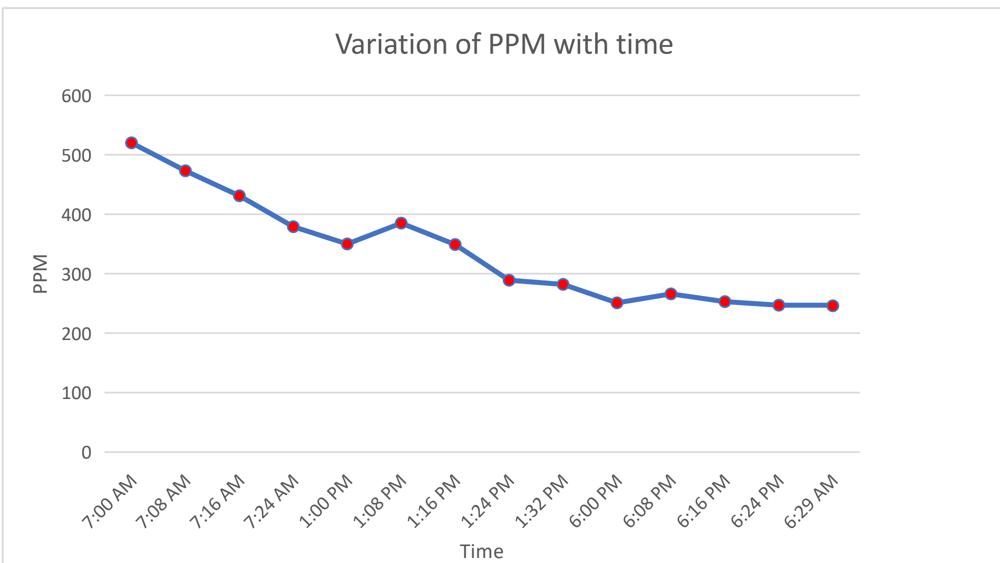

Figure 6. Variation of air quality with respect to time.

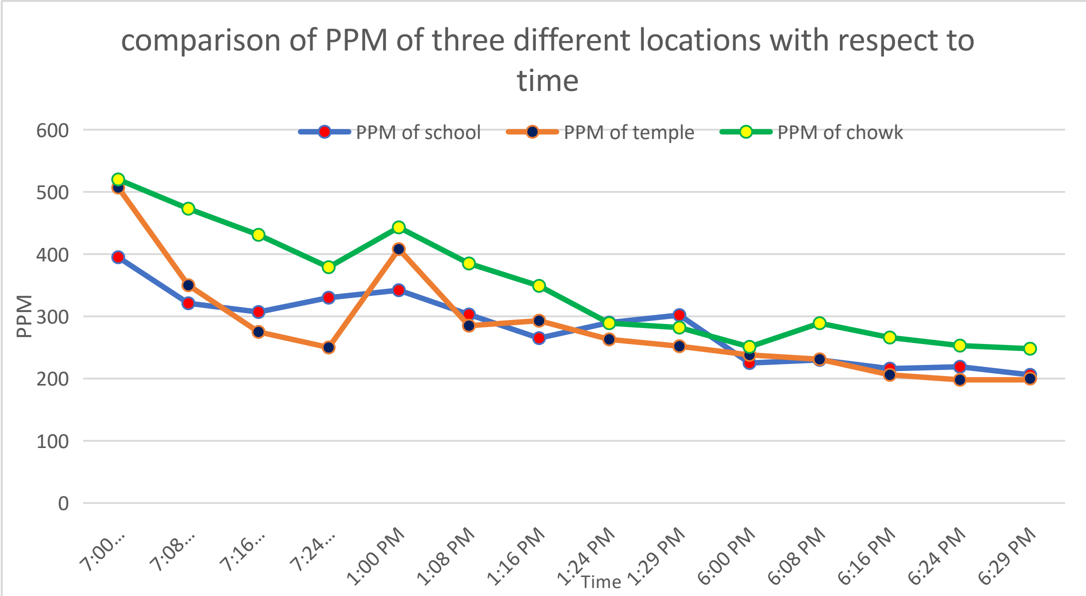

Figure 7. Comparison of PPM of three different locations with respect to time

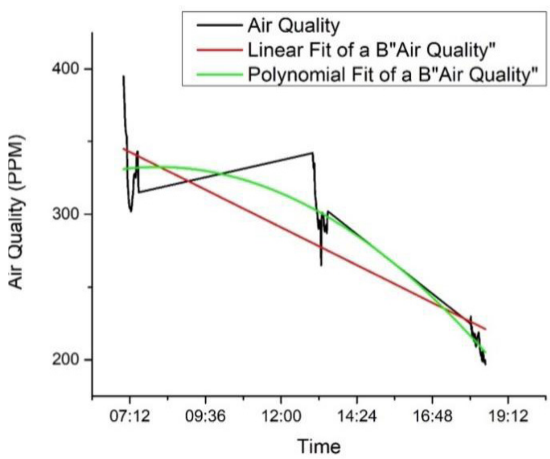

Figure 8. Graph showing the variation of PPM with time at school

Table 4. linear fitting of data obtained at school

Equation	y = a + b*x		
Residual Sum of Squares	51128.31124		
Pearson's r	–0.89729		
Adj. R-Square	0.80292		
		Value	Standard Error
Air Quality	Intercept	420.23025	7.71966
	Slope	–258.43197	13.55319

Table 5 represents the standard error of polynomial fitting of the data obtained at school.

Similarly, the analysis of data recorded from Buddha chowk is shown in the graph below:

Figure 9 shows the graph of linear fitting and polynomial fitting fitted between air quality (PPM) and time of Buddha Chowk. It analysed the data recorded at Buddha Chowk.

Table 5. Polynomial fitting of data obtained at school

Equation	y = Intercept + B1*x^1 + B2*x^2		
Residual Sum of Squares	26049.172		
Adj. R-Square	0.89844	Value	
		Value	Standard Error
Air Quality	Intercept	255.49572	18.8335
	B1	456.796	78.7527
	B2	–677.9677	74.07813

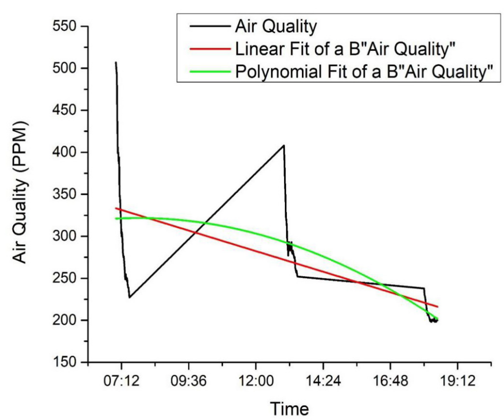

Figure 9. Graph showing the variation of PPM with time at Buddha chowk

This Table 6 below shows the standard error of linear fitting of the data obtained from Buddha chowk.

Table 6. Linear fitting of data obtained at Buddha chowk

Equation	y = a + b*x		
Residual Sum of Squares	271348.8699		
Pearson's r	–0.64166		
Adj. R-Square	0.40505		
		Value	Standard Error
Air Quality	Intercept	404.84907	17.78407
	Slope	–245.03894	31.22302

Table 7 shows the standard error of the polynomial fitting fitted using data of Buddha chowk.

Table 7. Polynomial fitting of data obtained at Buddha chowk

Equation	y = Intercept + B1*x^1 + B2*x^2		
Residual Sum of Squares	251342.58747		
Adj. R-Square	0.44258	Value	
		Value	Standard Error
Air Quality	Intercept	257.71558	58.50151
	B1	393.77057	244.62539
	B2	–605.53031	230.10503

Likewise, the analysis of the data recorded Khushi Khushi chowk at is shown in the graph below:

Figure 10 represents the graph of linear fitting and polynomial fitting fitted between air quality (PPM) and time of Khushi Khushi Chowk. It analysed the data of this location.

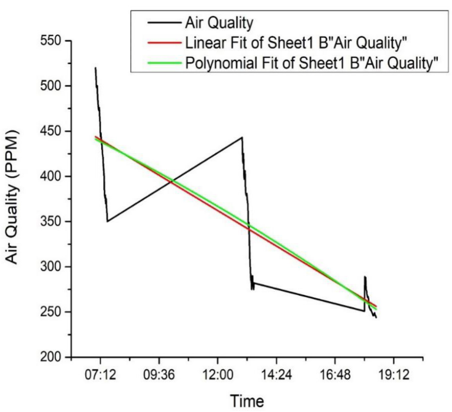

Figure 10. Graph showing the variation of PPM with time at Khushi chowk

The standard errors of linear fitting of the data obtained from Khushi Khushi chowk is shown in Table 8.

Table 8. Linear fitting of data obtained at Khushi Khushi chowk

Equation	y = a + b*x		
Residual Sum of Squares	153331.05743		
Pearson's r	–0.87192		
Adj. R-Square	0.75751		
		Value	Standard Error
Air Quality	Intercept	558.19117	13.36849
	Slope	–392.06105	23.47069

Table 9 represents the standard error of the data obtained from Khushi Khushi chowk after polynomial fitting.

Table 9. Polynomial fitting of data obtained at Khushi Khushi chowk

Equation	y = Intercept + B1*x^1 + B2*x^2		
Residual Sum of Squares	152331.02668		
Adj. R-Square	0.75633	Value	
		Value	Standard Error
Air Quality	Intercept	525.29578	45.54369
	B1	–249.23913	190.44197
	B2	–135.38151	179.1378

Analysis and comparison of data obtained from all three location are shown in graph below:

Figure 11 represents the graph of linear fitting and polynomial fitting fitted between air quality (PPM) and time all three locations. It shows the comparison of all three locations from where data are collected.

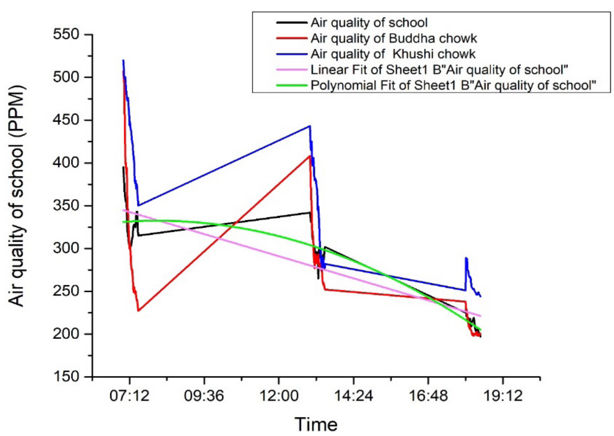

Figure 11. Graph showing the variation of PPM with time of all three locations

Table 10 shows the standard errors of linear fitting of the data obtained from all three locations .

Table 10. Linear fitting of data obtained from all three locations

Equation	y = a + b*x		
Residual Sum of Squares	51128.31124		
Pearson's r	–0.89729		
Adj. R-Square	0.80292		
		Value	Standard Error
Air Quality	Intercept	420.23025	7.71966
	Slope	–258.43197	13.55319

The standard errors of polynomial fitting obtained from data obtained from all three locations are shown in below Table 11:

Table 11. Polynomial fitting of data obtained from all three locations

Equation	y = Intercept + B1*x^1 + B2*x^2		
Residual Sum of Squares	26049.172		
Adj. R-Square	0.89844	Value	
		Value	Standard Error
Air Quality	Intercept	255.49572	18.8335
	B1	456.796	78.7527
	B2	–677.9677	74.07813

5. Conclusions

In this research, construction of "Air Pollution Monitoring System" based on Arduino Uno has been completed and measurement of air quality in PPM has been done by using the device. This "Air Pollution Monitoring System" works with a MQ 135 sensor and measures air quality of a specific location within the range of the sensor. It used Arduino Uno as a microcontroller which receives data collected by the sensor and display in the monitor as well as stored in the computer. I2C display has been used to monitored the air quality measured by the device. The device was constructed and tested.

To test the accuracy, reliability and validity of constructed device, data related to air pollution were recorded from three different locations, Basic Learning English Secondary School, Buddha Chowk periphery and Khushi chowk of Chandragiri-10, Boshigaun which lies within the southern part of Kathmandu. After collection of the data analysis of the data has been done. The data of air quality collected from these three locations have been fitted with linear line and polynomial curve using origin software. The standard error of linear fitting and polynomial fitting of air quality with respect to time has been done for the data of all three locations in the intercept.

The standard error of linear fitting and polynomial fitting of Basic Learning English Secondary School was obtained as 7.71966 and 18.8335 respectively. Similarly, the standard error of linear fitting and polynomial fitting of Buddha chowk periphery was found to be 17.78407 and 58.50151 respectively. Likewise, the standard error of linear fitting and polynomial fitting of Khushi chowk was obtained as 13.36849 and 45.54369 respectively.

In a nutshell, this device works perfectly for the measurement of air quality of a specific location within the range of sensor. The air quality of the observed locations is found to be less than 500 PPM in average. With the use of this device, the air quality of the locations that were under observations is found to be very good in average. It is found that the air quality of Chandragiri-10, Boshigaun is very good during evening time, normal during day time and a bit polluted during morning time. At last, this device works perfectly and can be used for the accurate and reliable data of air quality of specific location.

Conflict of Interest

There is no conflict of interest.

References

[1] Shah, H.N., Khan, Z., Merchant, A.A., et al., 2018. IOT Based Air Pollution Monitoring System. 9(2), 6.

[2] Air pollution, 2019. https://www.who.int/westernpacific/health-topics/air-pollution.

[3] Kim, S., Paulos, E., 2009. inAir: measuring and visualizing indoor air quality. Proceedings of the 11th international conference on Ubiquitous computing.

[4] Bashir Shaban, K., Kadri, A., Rezk, E., 2016. Urban Air Pollution Monitoring System With Forecasting Models. IEEE Sensors Journal. 16(8), 2598-2606. DOI: https://doi.org/10.1109/JSEN.2016.2514378

[5] Al-Dahoud, A., Fezari, M., Jannoud, I., et al., 2016. Monitoring Metropolitan City Air-quality Using Wireless Sensor Nodes based on ARDUINO and XBEE.

[6] Stojmenoviel, Handbook of sensor network, 1st ed. Ottawa: John Wiley and Sons, 2005.

[7] Kwon, J.W., Park, Y.M., Koo, S.J., et al., 2008. Design Of Air Pollution Monitoring System Using ZigBee Networks for Ubiquitous-City. Proceedings of the 2007 International Conference on Convergence Information Technology.

[8] Kathmandu Population, 2022. https://worldpopulationreview.com/world-cities/kathmandu-population.

[9] Guanochanga, B., Cachipuendo, R., Fuertes, W., et al., 2018. Real-time air pollution monitoring sys-

tems using wireless sensor networks connected in a cloud-computing, wrapped up web services. Proceedings of the future technologies conference (pp. 171-184). Springer, Cham.

[10] Meivel, S., Mahesh, M., Mohnish, S., et al., 2021. Air Pollution Monitoring System Using IOT And Artificial intelligence. International Journal of Modern Agriculture. 10(2), 2.

[11] Al Ahasan, Md.A., Roy, S., Saim, A.H.M., et al., 2018. Arduino-Based Real Time Air Quality and Pollution Monitoring System. International Journal of Innovative Research in Computer Science & Technology. 6(4), 81-86.
DOI: https://doi.org/10.21276

[12] Pal, P., Gupta, R., Tiwari, S., et al., 2017. IoT based air pollution monitoring system using Arduino. International Journal of Scientific Research in Science, Engineering and Technology. 4(10), 1137-1140.

[13] Jamil, M.S., Jamil, M.A., Mazhar, A., et al., 2015. Smart Environment Monitoring System by Employing Wireless Sensor Networks on Vehicles for Pollution Free Smart Cities. Procedia Engineering. 107, 480-484.
DOI: https://doi.org/10.1016/j.proeng.2015.06.106

[14] Zheng, K., Zhao, S., Yang, Z., et al., 2016. Design and Implementation of LPWA-Based Air Quality Monitoring System. IEEE Access. 4, 3238–3245.
DOI: https://doi.org/10.1109

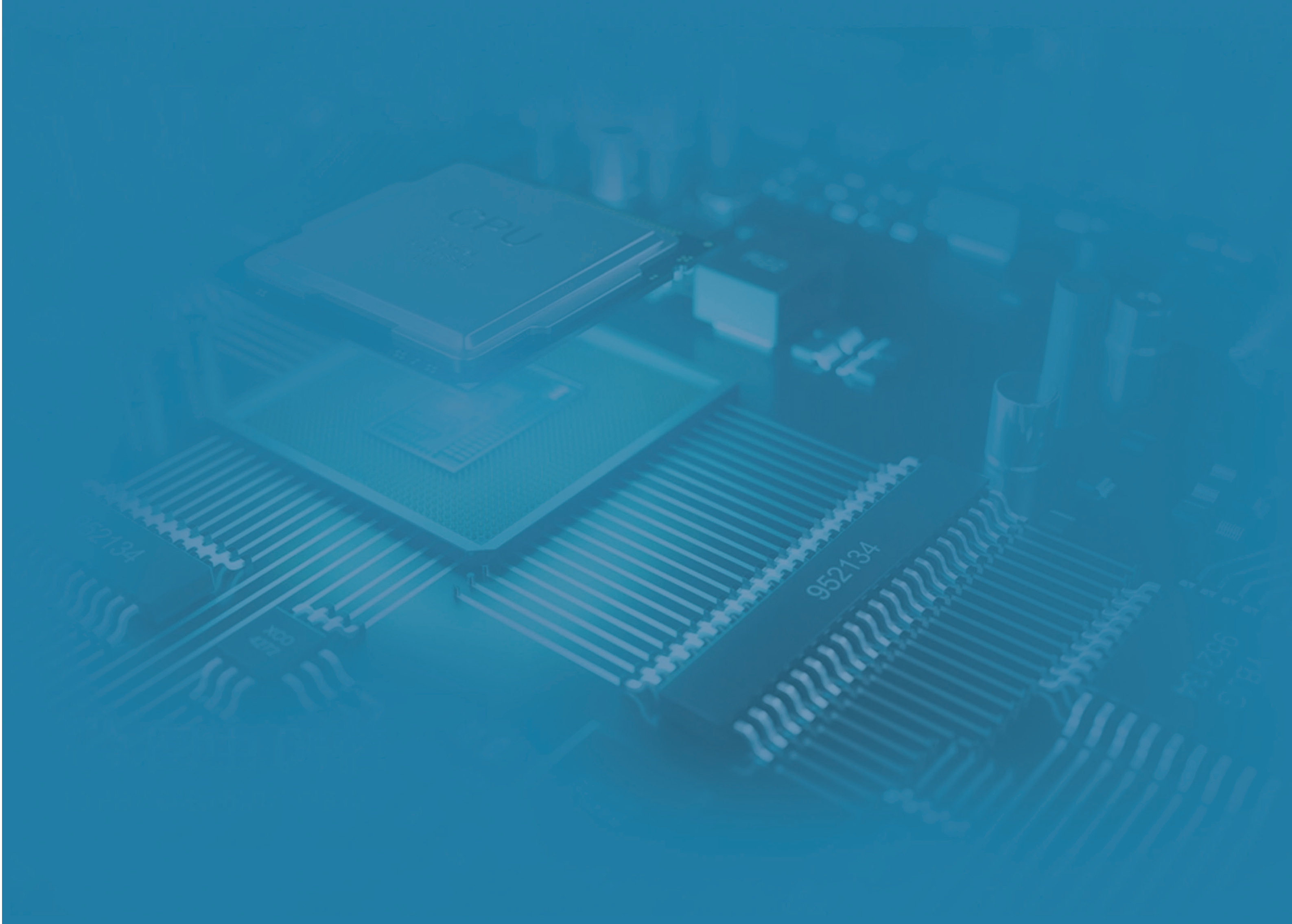

BILINGUAL PUBLISHING CO.
Pioneer of Global Academics Since 1984

Tel.:+65 65881289
E-mail: contact@bilpublishing.com
Website:ojs.bilpublishing.com

2661-3212